Marine and Petroleum Geology 140 (2022) 105633

Contents lists available at ScienceDirect

Marine and Petroleum Geology

journal homepage: www.elsevier.com/locate/marpetgeo

Marine redox evolution and organic accumulation in an intrashelf basin, NE Sichuan Basin during the Late Permian

Xiaotong Ge [a,b,c], Daizhao Chen [a,b,c,*], Gongjing Zhang [a,b,c,d], Taiyu Huang [a,b,c,e], Mu Liu [a,b], Moataz El-Shafeiy [a,b,f]

[a] Key Laboratory of Cenozoic Geology and Environment, Institute of Geology and Geophysics, Chinese Academy of Sciences, Beijing, 100029, China
[b] Innovation Academy for Earth Science, Chinese Academy of Sciences, Beijing, 100029, China
[c] University of Chinese Academy of Sciences, Beijing, 100049, China
[d] Shanxi Key Laboratory of Coal and Coal-measure Gas Geology, Department of Earth Science and Engineering, Taiyuan University of Technology, Taiyuan, 030024, China
[e] General Prospecting Institute, China National Administration of Coal Geology, Beijing, 100039, China
[f] Geology Department, Faculty of Sciences, Cairo University, Giza, 12613, Egypt

ARTICLE INFO

Keywords:
Late Permian
Organic accumulation
Redox condition
Marine productivity
Sea-level change

ABSTRACT

The Late Permian oceanic redox conditions are suggested to have had a causal relationship with the latest Permian mass extinction (LPME); however, the tempo-spatial variations of marine redox conditions which could have controlled environmental context of the LPME and organic accumulation remain loosely constrained. Here, we selected an organic-rich Lopingian succession deposited in an intrashelf basin, NE Sichuan Basin, SW China. To document the coeval oceanic changes, we present multiple geochemical proxies, including iron speciation, (major and trace) element contents, mercury (Hg) contents, total organic carbon contents (TOC) and carbonate carbon isotopic composition. Four intervals (I-IV) of discrete redox conditions were identified based on Fe–Mo–U–V datasets, revealing the evolutions from oxic to euxinic, and further to ferruginous conditions. Meanwhile, the primary productivity increased, then decreased in these intervals. The euxinic water wedge appeared in parallel with the high primary productivity and enrichment of organic matter, and advanced upslope and retreated downslope dynamically in the pace of sea-level rise and fall. In this case, marine redox variations were related to interactions of eustatic changes, organic decomposition, paleogeographic setting, upwelling currents, terrigenous input and volcanic activities. Compared with previous studies from other continents, it seems that the Paleo-Tethys was more anoxic and stagnant than Neo-Tethys and Panthalassa during the Late Permian, due to paleogeographic contexts and the more restricted oceanic circulation. In general, the prominent marine anoxia prevailed in the moderate water depth, and predated the major pulse of the LPME in several sections, which implies that anoxia may have not acted as the direct "killing mechanism" of this event.

1. Introduction

The Late Permian was a turning interval marked by dramatic oceanic, climatic, and geochemical changes in Earth's history, ending up with a mass extinction event accounting for a loss of more than 90% of marine organisms and over 70% of terrestrial vertebrates (Erwin et al., 2002; Sepkoski, 2016). These changes include large-scale perturbation of carbon cycling (Berner, 2002; Bond and Grasby, 2017), rapid global warming (Huey and Ward, 2005; Joachimski et al., 2012; Benton and Newell, 2014; Chen et al., 2020), ocean acidification and toxicity (Payne et al., 2010; Hinojosa et al., 2012; Black et al., 2014; Clarkson et al., 2015), and large-scale oceanic anoxia (Isozaki, 1997; Grice et al., 2005; Zhang et al., 2018a), accompanied with intense volcanic activities of the Large Igneous Province in Siberia (LIPS) (Svensen et al., 2009; Burgess et al., 2017) and/or South China (Gao et al., 2013; Zhao et al., 2019).

Over the past decades, numerous studies claimed that the widespread marine anoxia was the dominant killing mechanism for the latest Permian mass extinction (LPME) (Nielsen and Shen, 2004; Grasby and Beauchamp, 2009; Takahashi et al., 2014). Nonetheless, the anoxia was tempo-spatially heterogeneous across different depositional

* Corresponding author. Key Laboratory of Cenozoic Geology and Environment, Institute of Geology and Geophysics, Chinese Academy of Sciences, Beijing, 100029, China.
E-mail address: dzh-chen@mail.iggcas.ac.cn (D. Chen).

https://doi.org/10.1016/j.marpetgeo.2022.105633
Received 13 December 2021; Received in revised form 24 February 2022; Accepted 6 March 2022
Available online 9 March 2022

environments (or facies) in different continents (Dolenec et al., 2001; Fio et al., 2010; Clarkson et al., 2016; Elrick et al., 2017; Lei et al., 2017; Xiang et al., 2021), so that it was unlikely a direct cause of this event. Most of previous studies have focused mainly on the environmental changes across the Permian-Triassic (P-T) interval; however, less attention has been paid to the marine redox conditions prior to the P-T interval. This impedes the complete understanding of the oceanic context and the co-evolution of environmental-life processes and organic accumulation prior to the severest P-T biotic crisis.

Besides, the deep-water succession of Upper Permian in NE Sichuan Basin is organic-rich, acting as the high-quality source rock providing abundant hydrocarbons to the gasfields nearby (Cao et al., 2015; Wei et al., 2018). This facies-specific depositional succession archived abundant information associated with oceanic chemical and physical changes of the Late Permian which would be much helpful for understanding the oceanic factors controlling on the anomalous organic accumulation and evolving oceanic context predating the LPME.

To address the oceanic changes over the Late Permian, this study selected an organic-rich intrashelf basinal succession of the Upper Permian (upper Wuchiaping Formation, Dalong Formation and lowermost Feixianguan Formation in ascending order) at Xibeixiang, Guangyuan, NE Sichuan. Here, a series of analyses were carried out, including

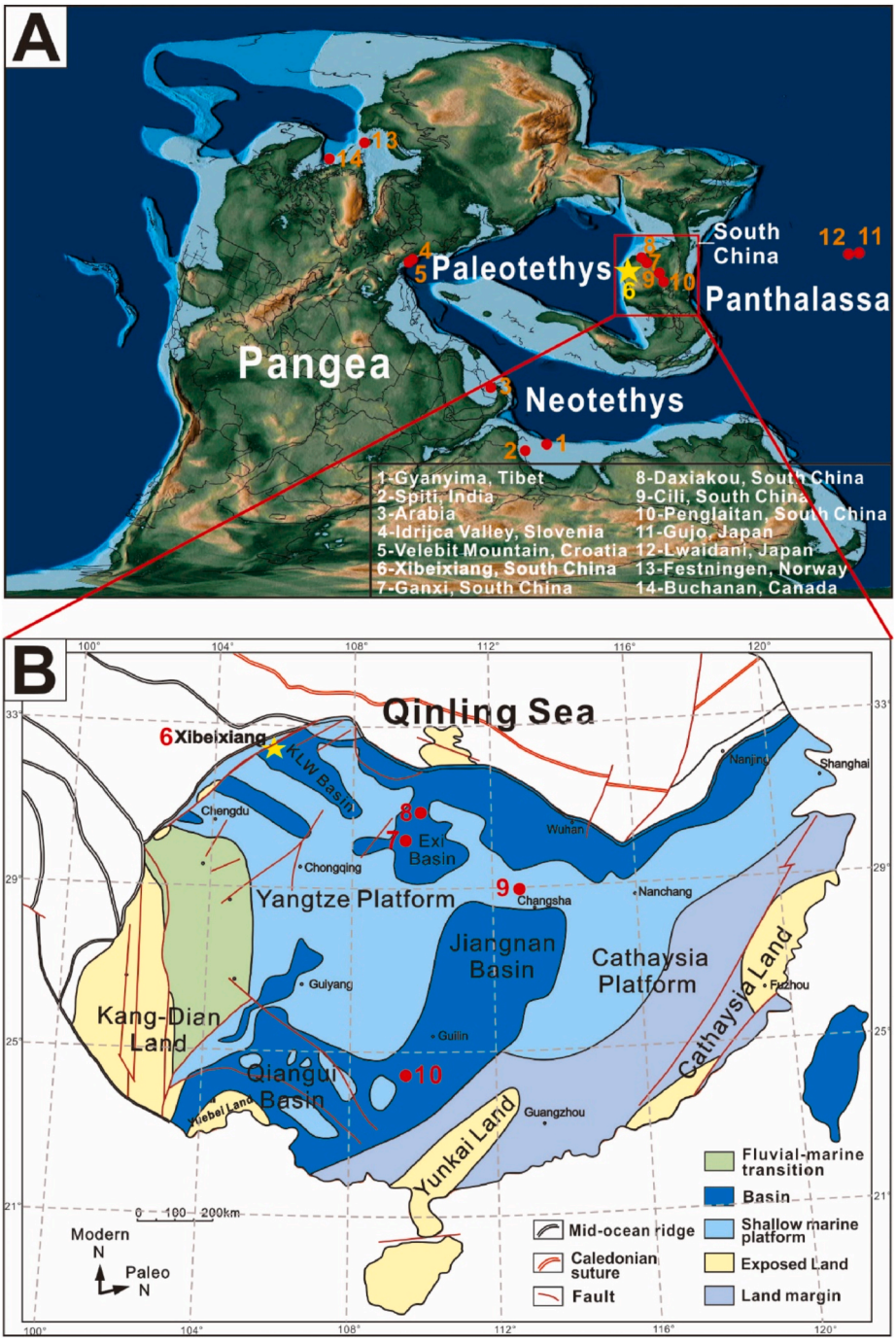

Fig. 1. (A) Paleogeographic map for the latest Permian showing the location of worldwide P-T sections and the present study section (modified from Scotese, 2016), (B) Paleogeographic map of the latest Permian of South China (KLW= Kaijiang-Liangping-Wangcang), showing the location of the Xibeixiang section (Star; modified from Luo et al., 2011).

iron speciation, major and trace element, Hg, total organic carbon contents (TOC), and carbon isotope composition. Based on these data, an integrated sedimentological, and geochemical profile upon the deep-water succession from the Lopingian to the P-T interval is constructed for the first time in the northwestern Yangtze Block. These datasets provide a more complete picture of the paleo-oceanic variations of the entire Late Permian in South China, facilitating better understanding of the abnormal organic enrichment and co-evolution of environment-life processes during this critical interval prior to the LPME.

2. Geological outline of the Lopingian (South China block)

The South China Block, amalgamated by the Yangtze and Cathaysia subblocks, was isolated from other continental blocks and migrated to

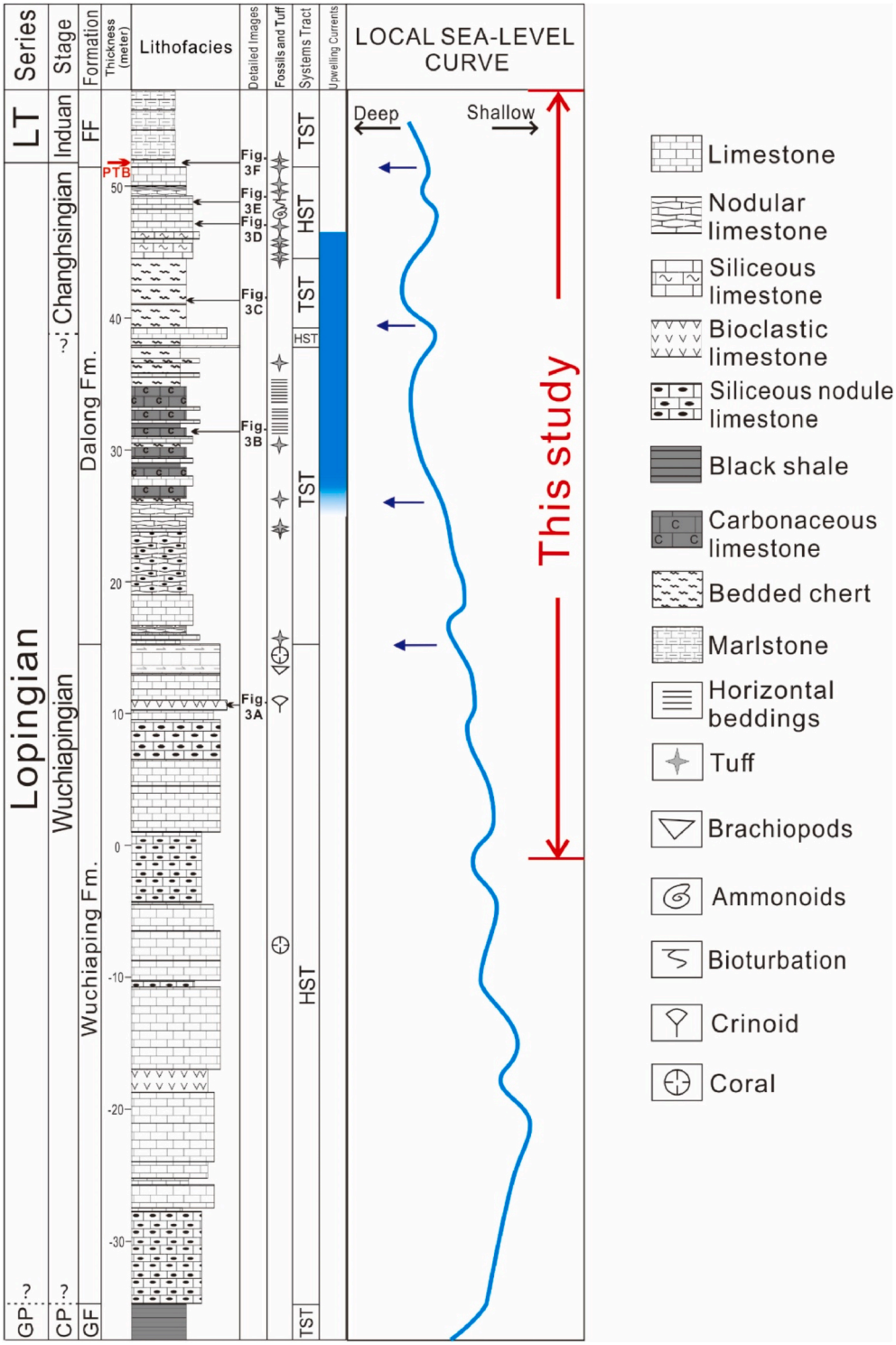

Fig. 2. Lithological column of Xibeixiang Section and sea level changes inferred from the vertical lithofacies changes. Abbreviations: GP-Guadalupian, CP-Capitanian, GF-Gufeng Formation, FF-Feixianguan Formation, LT-Lower Triassic, HST-highstand systems tract, TST-transgressive systems tract. The arrows mark apparent deepening processes (or sea level rise).

the subtropical latitude (approximately 23–25°N) of the Equatorial Warm Water Province (EWWP) during the Lopingian (Late Permian), forming the eastern margin of the Paleo-Tethys Ocean (Scotese and Langford, 1995; Mei and Henderson, 2001, Fig. 1A). During the Late Permian, carbonate platforms predominated over the Yangtze subblock, notably the upper Yangtze region, on which several intraplatform (or intrashelf) basins were developed (Fig. 1B). Paleogeographically, the Xibeixiang section was located near the mouth of the half-opened NW–SE trending Kaijiang-Liangping-Wangcang intraplatform basin linked to the Qinling Ocean (or Paleo-Tethys), which was proposed to be caused by the Emei Taphrogenesis (Shellnutt et al., 2012). It is about 35 km far from the Shangsi section northeastward sharing the similar depositional setting, which was once proposed as an auxiliary candidate of GSSP for the P-T boundary (Wignall et al., 1995).

At Xibeixiang, the well-exposed Upper Permian-Lower Triassic succession, overlying the Guadalupian Series, is composed of the Wuchiaping, Dalong and the lower Feixianguan formations in ascending order (Fig. 2). This study focuses on the succession starting from the upper Wuchiaping Formation, which consists of thick-bedded to massive bioclastic wackestones (Fig. 3A) with abundant shallow-water fauna (e.g., echinoid and brachiopod) and cherty (chalcedony) concretions/bands, representing a relative shallow-water environment (late high-stand systems tract-late HST). The Dalong Formation characterizes apparent lithological changes. The dominance of deep-water fauna assemblages (ammonoids and radiolarians) in the Dalong Formation (Fig. 2) is concordant with a deep-water intrashelf basinal environment (Cai et al., 2007; Yan et al., 2008). This formation approximately comprises three parts: the lower, middle and upper ones. The lower part is composed of thin- to medium-bedded lime mudstone/wackestone and thin-bedded siliceous mudstone, indicating a rapid deepening of water depth (onset of transgressive systems tract-TST). The overlying middle part is mainly composed of organic-rich marly limestone, intercalated with black shales/organic-rich limestones (Fig. 3B), indicating a progressive transgression (late TST). The uppermost limestone horizon thus represents a slight sea-level fall of HST. The upper part of the Dalong Formation, approximately corresponding to the Changhsingian Stage, is characterized by bedded cherts intercalated with shale partings in the base (Fig. 3C). It represents the onset of TST of late Lopingian. Upward, it is overlain by the limestone succession composed of thin- to medium-bedded lime mudstone (Fig. 3D) bearing nektonic ammonite fossils (Fig. 3E) and bioturbation, indicating a relative sea level fall (HST). The overlying Feixianguan Formation also marks an apparent lithological transition and is characterized by thin-bedded to platy marlstones or argillaceous lime mudstones intercalated with shaley partings, notably in the basal part (Fig. 3F), reflecting recurring sea-level rise (TST). It is worth to mention that up to 15 layers of bentonites are present, notably around the Permian-Triassic Boundary in Xibeixiang section (Figs. 2 and 3F), showing the direct evidence of volcanic

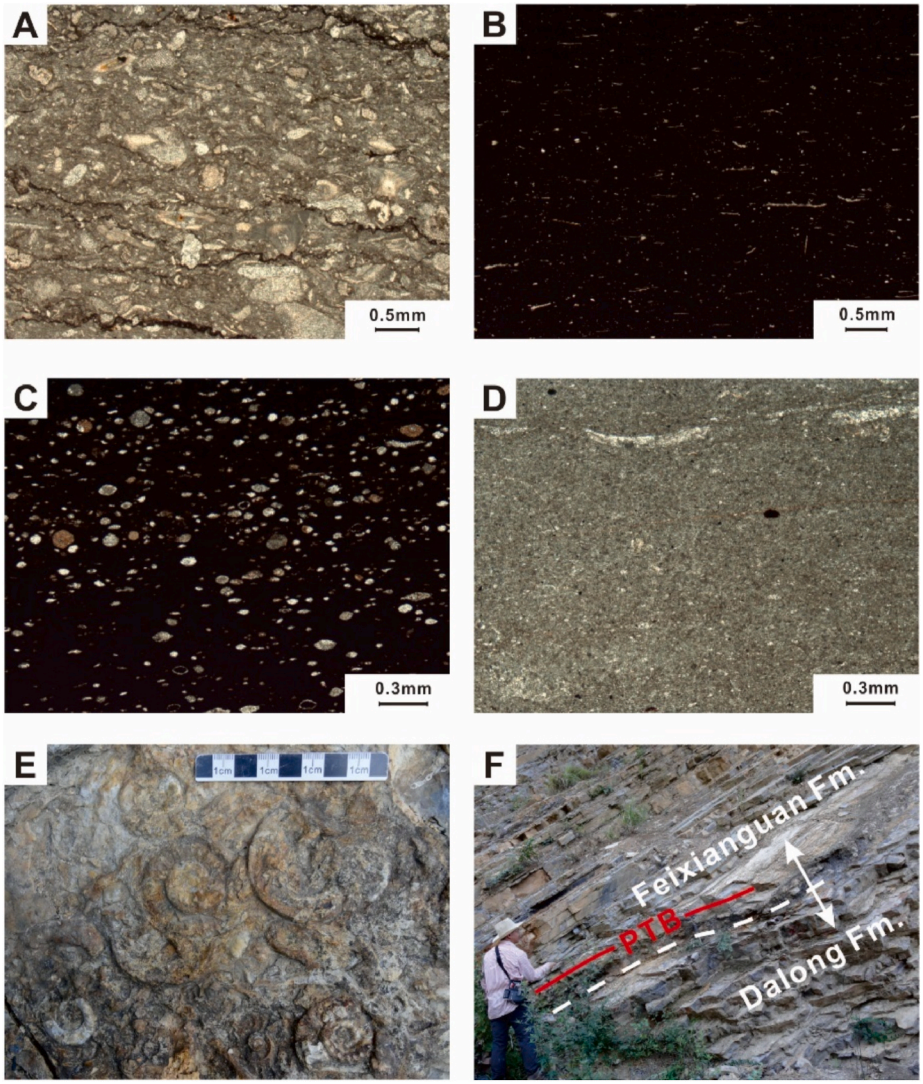

Fig. 3. Lithological features of Upper Permian at Xibeixiang. Photomicrographs (A-D) were taken under plane polarized light (A) Bioclastic wackestone bearing brachiopod and echinoid/crinoid fragments in the upper Wuchiaping Formation, (B) Carbonaceous limestone in the middle Dalong Formation, (C) Bedded chert bearing radiolarians in the upper Dalong Formation and (D) Lime mudstone in the uppermost Dalong Formation. (E) Ammonite fossils in the upper Dalong Formation. (F) Lithological variations across the Permian-Triassic boundary (PTB). Standing person for scale (1.65 m).

activities during deposition.

3. Materials and methods

A total of 79 samples were collected from Xibeixiang section, and all potential weathered surfaces, post-depositional veinlets or cavities, and visible nodules or bands were carefully removed from each sample. The samples were then cut into pieces with a hammer and further pulverized into powders of <200 mesh in size using Rocklabs BTRM apparatus. Homogenized powders were taken for subsequent analyses.

3.1. Major and trace elements analyses

For major elements, the lost-on-ignition (LOI) was calculated by the sample's mass difference between prior and after the combustion that can be used later for correction of the elemental abundances. 50 mg of each sample were weighed and dissolved in alkaline solution, followed by dilution of nitric acid and then determined by inductively coupled plasma optical emission spectrometer (ICP-OES) at China University of Geosciences (Beijing). The analytical accuracy monitored by the standards of AGV-2, GSR-1 and GSR-5 was >3%.

For trace elements, about 100 mg of each pulverized sample were dried at 980 °C for 1 h. Thereafter, aliquots of 40 mg of each sample were first treated with mixture solution of 1.5 ml concentrated HNO_3 and 1.5 ml HF, then heated at 195 °C for 48 h within sealed Teflon bombs. 1 ml HNO_3 was added to each sample that was further evaporated to incipient dryness, and then redissolved by 2 ml HNO_3 and 2 ml Milli-Q water and heated at 165 °C for 24 h to ensure complete digestion. Samples were diluted 4000-fold and conducted using inductively coupled plasma-mass spectrometry (ICP-MS) instrument at China University of Geosciences (Beijing). The analytical precision monitored by AGV-2, BHVO-2, W-2, GSR-1 and GSR-3 is generally >5%, except for (P and K) is <15%, and (Cr, Sc, Cu, Zn, Sr, and Ta) is <10%.

To subtract the terrigenous contribution and denote the authigenic component, trace element excess X_{XS} is calculated as follows: $X_{XS} = X_{sample} - Al_{sample} \times (X/Al)_{PAAS}$, where X_{sample} and Al_{sample} are the concentration of the element X and Al in samples and $(X/Al)_{PAAS}$ is the ratio of element X to Al in PAAS (Post-Archean Australian shale) (Taylor and Mclennan, 1985; Tribovillard et al., 2006). Likely due to the loss of authigenic components, there are negative Xxs values in some of the samples in this study. We uniformly set these negative values to 0.01 ppm to allow for convenient log10 plots of trace element excess versus depth.

3.2. Total organic carbon content

TOC analyses were conducted by the acid-wash method as described in (Wang et al., 2012). Aliquots of 200 mg of each sample were first treated twice with 6 N HCl for 24 h to dissolve any carbonate minerals. Samples were then washed with distilled water several times to remove any acid residue until pH > 5.0 and dried overnight (at 50 °C) before being weighed and powdered. Finally, the TOC was determined by Euro-EA3000 elemental analyzer at the Institute of Geology and Geophysics, Chinese Academy of Sciences (IGGCAS).

3.3. Carbon isotopes

Carbonate carbon isotopes were analyzed by Finnigan MAT-253 gas mass spectrometer at the Institute of Geology and Geophysics, Chinese Academy of Sciences (IGGCAS). 0.3–0.45 mg of sample powder was reacted with phosphoric acid at 72 °C and generated CO_2. Isotopic data were obtained by measuring CO_2. The results were reported in standard δ-notation relative to the Vienna Pee Dee belemnite (V-PDB). Analytical precision is better than 0.15‰.

3.4. Iron speciation

The mass fractions of carbonate-associated (Fe_{carb}), (oxyhydr)oxide (Fe_{ox}), and magnetite-associated (Fe_{mag}) iron phases were analyzed sequentially following the procedure of Poulton and Canfield (2005b). Only samples with total iron (Fe_T) > 0.5% were selected for iron speciation analysis (note: all concentrations are weight percent unless otherwise noted). 100 mg of rock powders were used for Fe_{carb} extraction by sodium acetate solution buffered to pH = 4.5 with analytical-grade acetic acid in 50 °C water-bath for 48 h. The remaining part of the samples after the first step were treated with sodium dithionite solution buffered to pH = 4.8 by addition of 0.2 M sodium citrate and trace-metal grade acetic acid in a 50 °C water-bath for 2 h to extract Fe_{ox}. The remaining residue was further extracted for Fe_{mag} using mixed solution of 0.2 M ammonium oxalate and 0.17 M oxalic acid (pH = 3.2, 50 °C, 6 h). After being diluted with 2% HNO_3, all the extracted fractions were measured for Fe content using atomic absorption spectroscopy (AAS), yielding an RSD of <5% at the State Key Laboratory of Biogeology and Environmental Geology, China University of Geosciences (Wuhan). On the other hand, pyrite iron (Fe_{py}) was extracted following the chromium reduction method (Canfield et al., 1986). Approximately 1–3 g of decarbonated sample powders were reacted with boiling 1 M $CrCl_2$ solution (200 ml) under N_2 for 2 h. The liberated hydrogen sulfide (H_2S) gas was trapped in 20 ml of 10 wt% $AgNO_3$ solution as Ag_2S precipitates. After filtration, drying, and homogenization of the precipitates, the mass fraction of Fe_{py} was calculated stoichiometrically from Ag_2S. The analysis was carried out at the Institute of Geology and Geophysics, Chinese Academy of Sciences (IGGCAS). Highly reactive iron (Fe_{HR}) was calculated as the sum of Fe_{carb}, Fe_{ox}, Fe_{mag}, and Fe_{py}. Total iron (Fe_T) is obtained from the content of Fe_2O_3 in major element data.

3.5. Hg content

Prior to Hg analysis, the sample powders were dried at 50 °C for 2 h. Mercury concentration was measured using a Lumex RA-915+ Hg analyzer equipped with a pyrolysis attachment at the Institute of geochemistry, Chinese Academy of Sciences (IGCAS). Standards were measured after every 10 samples to ensure the reliability of the data using GBW07405 (GSS-5) as the Hg standard, and coefficients of variation for triplicate analyses were <6%.

4. Results

The main geochemical data from the Xibeixiang section are presented in the supplementary file (Supporting Information), and illustrated in Figs. 4 and 5.

Carbonate carbon isotope data ($\delta^{13}C_{carb}$) vary from −6.02‰ to 4.57‰, showing three perturbations in the studied succession (Fig. 4): a negative excursion (nadir around −6.02‰) in middle Dalong Formation and a positive anomaly (maximum at 1.62‰) in upper Dalong Formation, which is followed by a rapid negative shift near the P-T boundary. The TOC contents range from 0.03 to 13.68 wt% (mean 2.37 wt%), which are particularly high in the middle of Dalong Formation.

Total Fe (Fe_T) concentrations range from 0.06 to 6.20 wt% (average 1.11 wt%), but it is noteworthy that most samples in the upper Wuchiaping Formation and the lower Dalong Formation yield values lower than 0.5 wt%. Their changes generally follow the patterns of TOC variations, except for data in Feixianguan Formation (Fig. 4). For those samples with Fe_T > 0.5 wt%, Fe_{HR}/Fe_T ratios vary from 0.28 to 0.83 (average 0.62), while Fe_{py}/Fe_{HR} ratios vary from 0.01 to 0.94 (average 0.64).

Mo_{XS} concentrations range from 0.52 to 804.05 ppm (mean 35.85 ppm), and show a similar variation pattern with Fe_{py}/Fe_{HR} ratios (Fig. 4). Mo/TOC ratios fluctuate between 1.37 and 101.37 ppm/wt% (mean 20.46 ppm/wt%). Moreover, $[U_{XS}]$ vary from 0.01 to 81.54 ppm

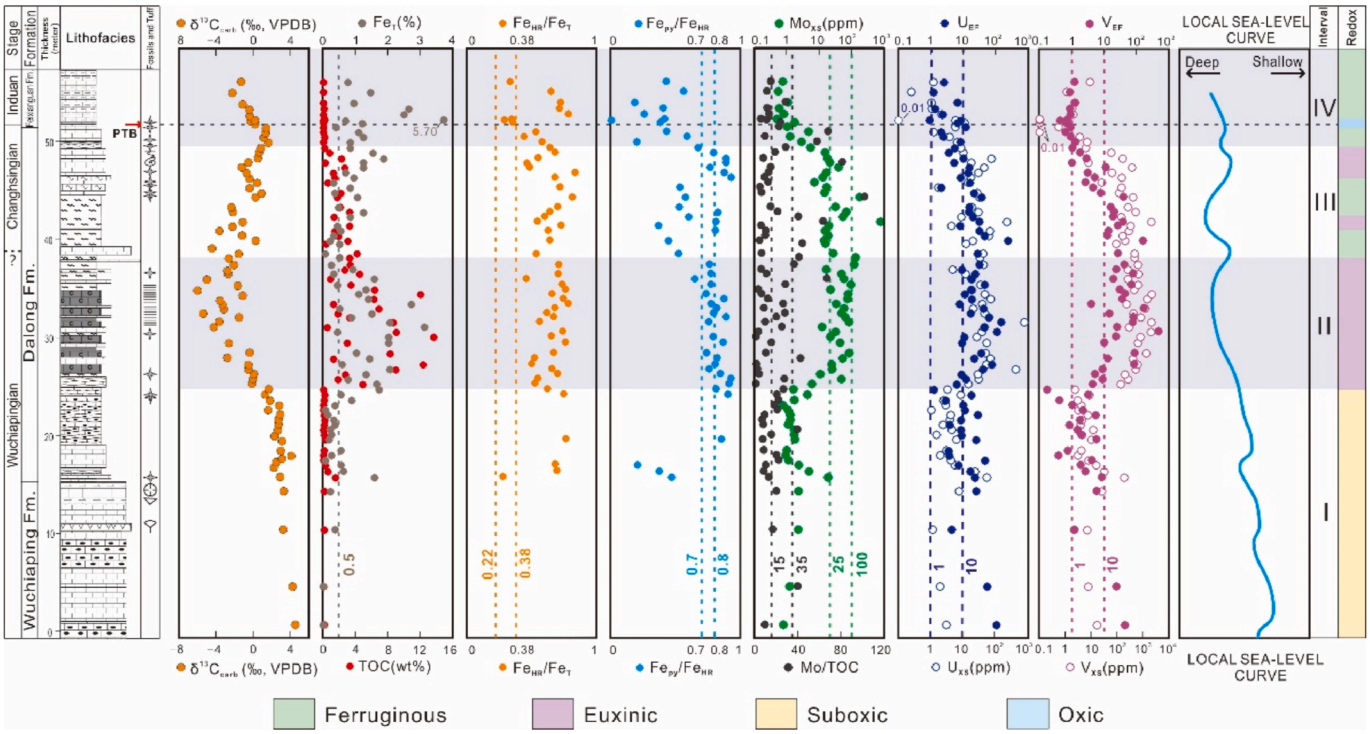

Fig. 4. Stratigraphic variations of $\delta^{13}C_{carb}$, TOC, Fe speciation, and other redox proxies in the Xibeixiang section. Vertical dashed lines in each column mark key threshold values of Fe speciation and redox-sensitive trace element proxies documented in the text. See Fig. 2 for lithologies.

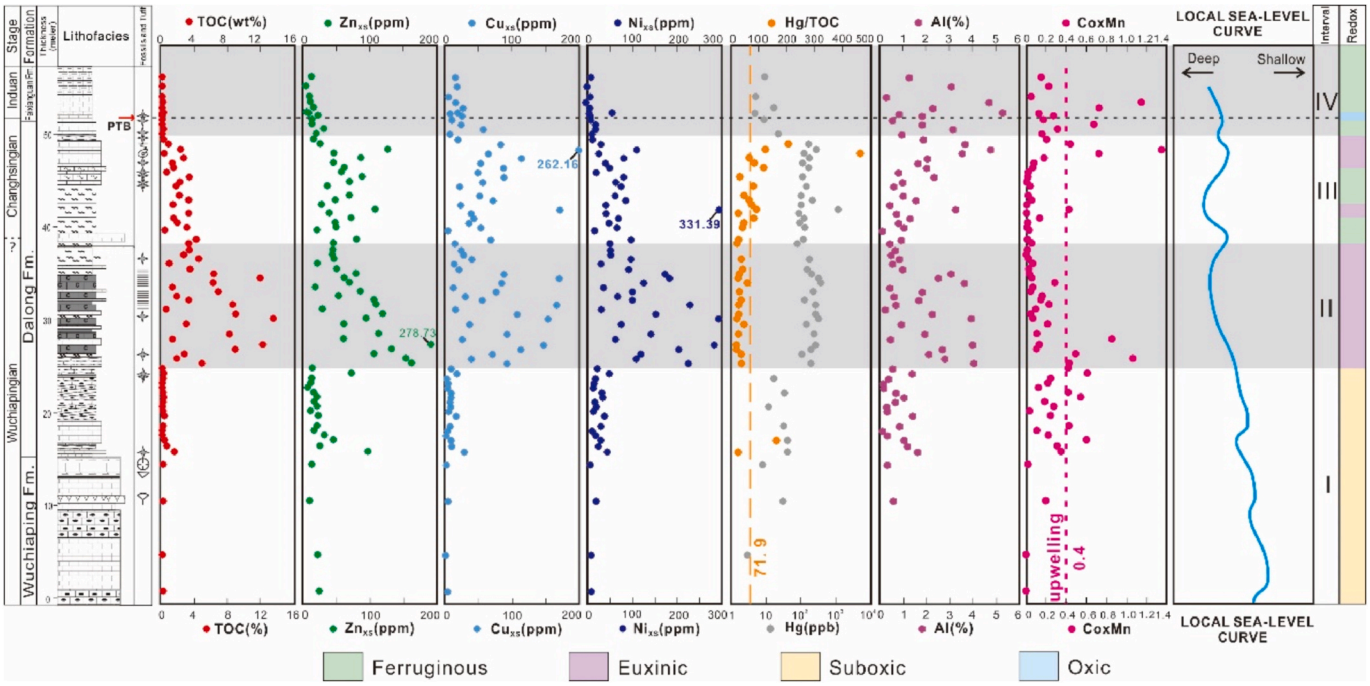

Fig. 5. Vertical variations of proxies of primary productivity (TOC, Zn_{XS}, Cu_{XS}, and Ni_{XS}), volcanic activity (Hg abundance and Hg/TOC ratios), terrigenous input (Al contents) and upwelling currents (Co × Mn) in the Xibeixiang section. See Fig. 2 for lithologies.

(mean 6.87 ppm), U_{EF} vary from 0.91 to 347.79 (mean 24.78), [V_{XS}] vary from 0.01 to 2174.98 ppm (mean 322.39 ppm) and V_{EF} vary from 0.51 to 200.01 (mean 19.69). All U_{XS}, V_{XS}, U_{EF} and V_{EF} values display similar variation patterns of Fe_{py}/Fe_{HR} ratios that stay relatively high in the middle part of Dalong Formation (Fig. 4).

As for nutrient elements (Fig. 5), [Zn_{XS}], [Cu_{XS}] and [Ni_{XS}] range from 3.57 to 278.73 ppm, 0.54 to 262.16 ppm and 0.01 to 331.39 ppm, respectively, following an approximately similar trend maximizing in the middle part of Dalong Formation. Similarly, Hg concentrations vary from 2.92 to 1174.19 ppb (mean 149.34 ppb), reaching relatively high in the mid-upper Dalong Formation. In contrast, Hg/TOC ratios are generally downward-flattening from 21.38 to 463.25 ppb/wt% (mean 101.23 ppb/wt%), although an abrupt increase was created near the P-T boundary. Moreover, Al concentrations vary from 0.04 to 5.62 wt%

(mean 1.62 wt%), maximizing around the P-T boundary. While Co × Mn values range from 0.0037 to 2.87 ppm·wt% (mean 0.27 ppm·wt%), staying fairly low in the mid-upper Dalong Formation.

5. Discussion

5.1. Marine redox conditions of Late Permian

According to Tyson and Pearson (1991), paleo-redox states of water media can be differentiated into oxic, suboxic, anoxic, and euxinic conditions. Iron speciation has been widely used to evaluate paleo-oceanic redox conditions under which the fine-grained siliciclastic sediments were deposited. During silicification and dilution of siliciclastic sediments, Fe is a conservative element without significant migration, and remains relatively stable (e.g., Yuan et al., 2014). In this light, iron speciation is applicable for fine-grained siliciclastic rocks, since dilution works consistently onto all iron species.

In modern oxic water columns, Fe_{HR} in sediments makes up less than 38% fraction of Fe_T, so that if sediments yield a Fe_{HR}/Fe_T ratio of $\geq$0.38, an anoxic state is indicated in which as if the Fe_{py}/Fe_{HR} ratio is $\geq$ 0.8, a euxinic (or sulfidic) condition is further differentiated from the ferruginous-dominant anoxia. Furthermore, an intermittent euxinic state may have been indicated as if the Fe_{py}/Fe_{HR} ratios vary between 0.7 and 0.8, notably from deep-time rocks (Poulton and Canfield, 2005a, 2011). These proxies work efficiently only as if Fe_T > 0.5%, even in carbonate rocks (Clarkson et al., 2014).

Several redox-sensitive trace elements (e.g., U, V and Mo) are also commonly used as tracers to reconstruct the paleo-redox history in deep time, because these elements are less soluble under oxygen-depleted marine environments (Calvert and Pedersen, 1993; Algeo and Maynard, 2004; Tribovillard et al., 2006), which allow us to investigate changes in redox conditions in ancient sedimentary archives. Under reducing conditions, U(VI) can be reduced to insoluble U(IV) and precipitate below the Fe(III)–Fe(II) redox boundary (Tribovillard et al., 2006). As for Vanadium, soluble V(V) is reduced to V(IV) under a mildly reducing condition, such as $VO(OH)^{3-}$ and insoluble hydroxides $VO(OH)_2$. Under euxinic conditions, the presence of free H_2S can cause V(IV) to be further reduced to V(III), which can be absorbed by the geoporphyrins complex or precipitated as the solid oxides (Breit and Wanty, 1991; Wanty and Goldhaber, 1992). Besides, molybdate can be converted to particle reactive thiomolybdate in the presence of free H_2S under the anoxic water column, resulting in rapid removal of dissolved Mo from the water into sediments by organic matter or sulfide minerals (Algeo and Lyons, 2006). Studies on modern marine sediments show that Mo concentrations in sediments are commonly higher than 100 ppm under permanent euxinic conditions, and vary between 25 ppm and 100 ppm under intermittently euxinic conditions or permanently Mo-depleted euxinic conditions, and remain lower than 25 ppm under non-euxinic conditions (Scott and Lyons, 2012).

However, it is noteworthy that other factors may have also affected Mo enrichment. Firstly, the so-called "basin reservoir effect" resulting from insufficient Mo renewal in the highly restricted basins could draw down the deep-water aqueous Mo concentrations (Tribovillard et al., 2006). Furthermore, the Mo in water column can be scavenged and trapped by Fe (oxyhydr)oxides and Mn oxides through adsorption in sediments under an oxic-suboxic water column (Scholz et al., 2017; Ho et al., 2018; Scholz, 2018), thus Mo burial fluxes may be higher than expected in weakly anoxic (or sulfidic) environments and lower than anticipated in strongly sulfidic environments. In this light, we thus dominantly rely on the Fe speciation to infer the marine redox conditions in this study, integrated with trace element (U, V and Mo) proxies after careful evaluation of the consistency among different proxies.

Four discrete intervals (I-IV) are identified based on integrated redox proxies (Fig. 4). Interval I (0–23.95 m at height) is located in the lower part of the section, spanning from the upper Wuchiaping Formation to the lower Dalong Formation. In this interval, the relatively depleted Fe_T (mostly lower than 0.5 wt%) contents make Fe-specified redox proxies somewhat uncertain, although a few samples with Fe_T > 0.5 wt% denote an oxygen-deficient environment (Fe_{HR}/Fe_T > 0.38). However, the U, V and Mo are only weakly enriched in this interval (mean $[U_{XS}]$ 2.15 ppm, mean U_{EF} 19.63, mean $[V_{XS}]$ 17.54 ppm, mean V_{EF} 4.46, mean $[Mo_{XS}]$ 2.72 ppm). Collectively, these redox signals suggest a suboxic water column during deposition.

Interval II (23.95–37.38 m at height) is posited in the middle Dalong Formation. In this interval, almost all samples contain sufficient Fe_T (>0.5 wt%), and yield Fe_{HR}/Fe_T > 0.38 (Fig. 4), indicating an anoxic condition, consistent with the enrichment of U (mean $[U_{XS}]$ 12.97 ppm, mean U_{EF} 42.27) and V (mean $[V_{XS}]$ 761.70 ppm, mean V_{EF} 43.89). Most of Fe_{py}/Fe_{HR} ratios are greater than 0.7, revealing a euxinic-dominant water condition. Moreover, $[Mo_{XS}]$ are mostly between 25 and 100 ppm (mean 55.47 ppm), which may reflect a euxinic-dominant environment in a semi-restricted basin. Therefore, we infer a euxinic condition during this interval.

Upwards to interval III (37.38–48.54 m at height) in the upper Dalong Formation (Fig. 4), samples have Fe_{HR}/Fe_T > 0.38, suggesting an anoxic watermass; while Fe_{py}/Fe_{HR} ratios are fluctuating around 0.7 (0.37–0.94, mean 0.70), implying intermittent incursions of euxinic watermasses into the ferruginous-dominant water column. This scenario generally agrees with relatively high $[U_{XS}]$ (mean 7.53 ppm), U_{EF} (mean 20.69), $[V_{XS}]$ (mean 287.20 ppm), V_{EF} (mean 16.75) and $[Mo_{XS}]$ (mean 67.68 ppm) although moderate declining related to interval II. It is noted that the euxinic water column recurred at the end of this interval concordant with the high Fe_{py}/Fe_{HR} ratios (>0.8). Therefore, Interval III likely experienced ferruginous-dominant anoxic condition with intermittent incursions of euxinic water.

Further upwards to Interval IV (48.54–55.24 m, the lowermost Feixianguan Formation), samples yield Fe_T > 0.5 wt% and most of which have Fe_{HR}/Fe_T ratios >0.38 (0.28–0.78, mean 0.52) with Fe_{py}/Fe_{HR} ratios <0.7 (0.01–0.60, mean 0.36) (Fig. 4), indicating a predominance of ferruginous anoxic condition. This scenario generally reconciles the variations in $[U_{XS}]$, U_{EF}, $[V_{XS}]$, V_{EF} and $[Mo_{XS}]$ values (Fig. 4). However, samples just at the P-T boundary yield Fe_{HR}/Fe_T ratios less than 0.38, manifesting a short oxic spell. This inference is well in agreement with the drastic drops in U_{XS}, V_{XS} and Mo_{XS} concentrations (Fig. 4). Thus, a ferruginous state may have predominated over this interval, interrupted by an oxic spell just across the P-T transition.

Furthermore, the weak correlations among Mo_{XS}, U_{XS}, and Fe_{py}/Fe_{HR} ratios versus TOC contents (Fig. 6) suggest that a weak linkage between the redox condition of water column and organic matter accumulation during the Late Permian at Xibeixiang.

5.2. Primary productivity

The output of organic carbon onto the seafloor is function of the primary productivity in the surface water to some extent (Pedersen and Calvert, 1990; Canfield, 1994; Tyson, 2005). Several geochemical proxies such as P, Ba, Zn, Cu and Ni abundances in organic matters are somewhat related to the primary bioproductivity of phytoplankton, thereby being used as the tracers to assess the primary productivity in some specific cases (Tribovillard et al., 2006; Piper and Calvert, 2009).

Phosphorus can be deposited in association with decayed microorganisms (Filippelli and Delaney, 1996; Schenau and Lange, 2001; Schenau et al., 2005). Theoretically, oxygenated conditions tend to promote phosphorus retention by adsorption onto the Fe–Mn (oxyhydro-)oxides within sediments such that P_{XS} contents tend to be proportional to the primary productivity in an oxic environment (Cappellen and Ingall, 1994; Schoepfer et al., 2015). In contrast, P can be recycled from organic matter into the reducing water column, resulting in lower P_{XS} contents (or P depletion) in sediments even with a high bioproductivity (Schenau and Lange, 2001; Algeo and Ingall, 2007). In turn, a permanently sulfidic bottom water could impede the precipitation of Fe-oxyhydroxides there, reducing the potential for their

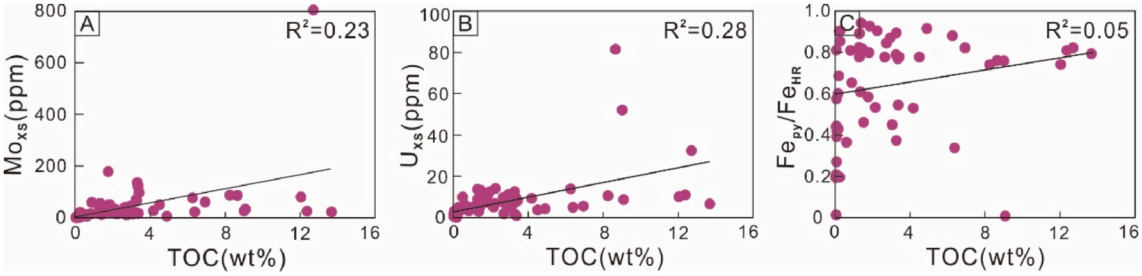

Fig. 6. Crossplots of Mo_{XS}, U_{XS}, and Fe_{py}/Fe_{HR} contents versus total organic carbon (TOC) contents in the Upper Permian succession at Xibeixiang section.

adsorption and complexation of the re-mineralized organic P (Tribovillard et al., 2006), limiting direct usage of P abundance as a productivity proxy in organic-rich sediments.

Similarly, although the Ba_{XS} flux, the indicator of the amount of microcrystal barite rain fallout in the water column, highly depends on the primary productivity (Bishop, 1988; Schmitz, 1987), the redox states of bottom water or porefluid in sediments, notably the anoxic watermass, would favour the bacterial sulfate reduction (barite dissolution), drawing down the Ba contents in sediments. Therefore, both P and Ba have lower preservation efficiency in anoxic conditions, limiting direct usage of P and Ba abundances as productivity proxies (Dehairs et al., 1980, 1987, 1992; Dymond et al., 1992).

Zinc, copper and nickel are micronutrient-limiting elements and their authigenous fractions are proportional to primary productivity (Algeo and Maynard, 2004; Piper and Perkins, 2004). They are absorbed by micro-organisms through photosynthesis of primary producers before deposition. Subsequently, as the organic matter is partly or completely decomposed, Zn, Cu and Ni could be released to the overlying watermass and potentially to form sulfides in an H_2S-containing water column, thereby preserving in sediments (Algeo and Maynard, 2004; Piper and Perkins, 2004). As discussed above in Section 5.1, an oxygen-deficient even euxinic condition dominated the intrashelf basin in the Late Permian (Fig. 4). Therefore, only Zn_{XS}, Cu_{XS} and Ni_{XS} can be used as the proxies for paleo-productivity.

It is well demonstrated that [Zn_{XS}], [Cu_{XS}], and [Ni_{XS}] coherently vary with TOC changes in the Upper Permian succession at Xibeixiang (Figs. 5 and 7), pointing to a deterministic contribution of increased bioproductivity to the organic output and accumulation such that they are efficient indicators of bioproductivity. More specifically, tied to the redox intervals as documented above (Section 5.1), these proxies ([Zn_{XS}], [Cu_{XS}], and [Ni_{XS}]) stay fairly low in interval I, and culminate in interval II, which are then followed by an episodic decrease in interval III, and remain lowstand in interval IV (Fig. 5). Accordingly, a low productivity rate is indicated in interval I and increasing productivity in interval II, which then is followed by episodic decreases in interval III and remain persistent low in interval IV.

5.3. *Influence of volcanic activities*

Intense volcanic activities may cause major perturbations to terrestrial and marine ecosystems, and global biogeochemical cycles, due to inputs of both toxic and nutrient substances, and releasing of greenhouse gases (CO_2, CH_4 and SO_2) into Earth surface system (Grasby et al., 2017). The enhanced volcanic activity was widely suggested as the trigger for inducing the oceanic anoxic events (OAEs) in geological history (Percival et al., 2015; Scaife et al., 2017; Charbonnier et al., 2018). In recent years, mercury (Hg) abundance and its isotope systematics have been increasingly used as a new alternative proxy to trace the volcanic activities in deep geological times (Grasby et al., 2013, 2017; Percival et al., 2015; Sial et al., 2016), providing the linkage of environmental-life coevolution on Earth surface to the Earth's internal process (Sanei et al., 2011; Thibodeau et al., 2016; Percival et al., 2017).

The volcanic flux of Hg is thought to be the largest source of non-anthropogenic Hg input (Pirrone et al., 2010). Hg was washed out from the atmosphere and/or terrestrial riverine runoff and then entered aqueous media (Gill and Fitzgerald, 1988; Holmes et al., 2010; Amos et al., 2014). Subsequently, Hg was precipitated mainly in organic matter, sulfides and clay minerals through forming organic–Hg complexes, HgS, or adsorption, resulting in a high affinity of Hg to TOC, total sulfur (TS) and Al (Benoit et al., 1999; Ravichandran, 2004; Bower et al., 2008; Bouffard and Amyot, 2009; Selin, 2009; Han et al., 2014; Duan et al., 2016). In order to precisely evaluate Hg anomalies, it is necessary to determine the main occurrence forms and controlling factors of Hg.

Our data from Xibeixiang section show that Hg contents are proportional to TOC contents in most samples, but are poorly correlated with Al and TS (Fig. 8), indicating that Hg resides mainly in the form of organics–Hg complexes in sediments. To buffer the overwhelming influence of TOC contents on the Hg anomalies, the Hg contents are normalized to the TOC contents (Hg/TOC) which average 71.9 ppb/wt.% in sediments (Grasby et al., 2019). However, if TOC values are lower than the analytical uncertainty (0.2 wt%), the Hg anomalies should be questioned (Grasby et al., 2013).

In intervals I and IV, most of TOC contents are lower than 0.2 wt%, hence Hg/TOC ratios are not adopted. Although Hg concentrations remain high in both intervals II and III, Hg/TOC ratios are flattened, except a few positive anomalies on the top of interval III (Fig. 5), indicating intensified volcanic activities that time. This scenario agrees with concentrated occurrences of tuffaceous (bentolite) layers across the boundary of Dalong and Feixianguan formations (Fig. 3A). In addition, this Hg/TOC anomaly has been reported from more than 20 localities

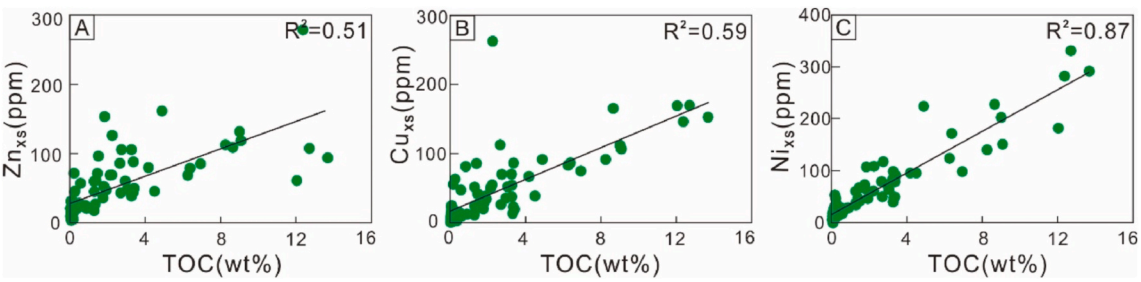

Fig. 7. Crossplots of Zn_{XS}, Cu_{XS}, and Ni_{XS} contents versus total organic carbon (TOC) contents in the Upper Permian succession at Xibeixiang section.

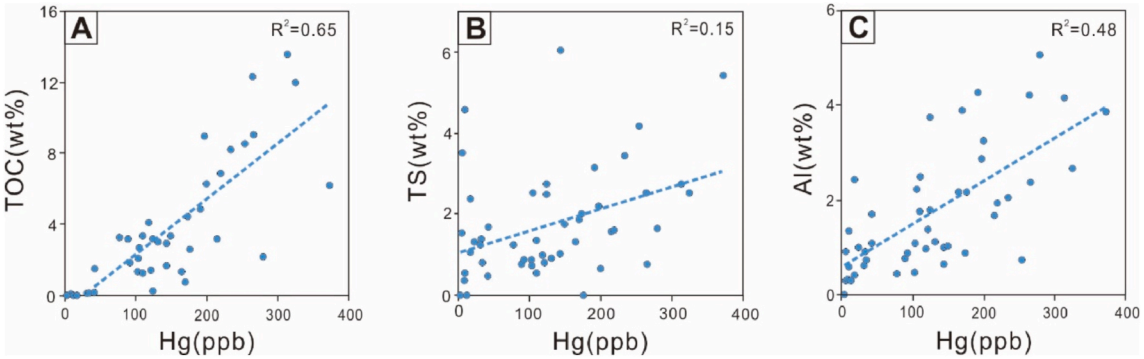

Fig. 8. Cross-plots of (A) Hg vs. TOC, (B) Hg vs. TS, (C) Hg vs. Al in studied interval.

over the world in the time-equivalent horizons of the uppermost Permian, indicating a widespread volcanic activity near the end-Permian (Sanei et al., 2011; Grasby et al., 2013, 2017; Wang et al., 2018a, 2019; Shen et al., 2019a, 2019b). Whether this volcanic signature recorded on South China block was derived from the arc volcanisms around South China block or the Siberia Large Igneous Provinces (SLIPS) still remains controversial (Gao et al., 2013; Burgess et al., 2017; Zhao et al., 2019). Nevertheless, more and more studies suggested that these volcanic materials were probably from the subduction-zone magmatic arcs along the margins of the South China Craton, as evidenced by the crystal fragments, age spectrum of zircons, Cu concentration and isotope anomalies, Hg isotopes and the spatial distribution of particle sizes (Gao et al., 2013; Wang et al., 2018b; Zhao et al., 2019; Zhang et al., 2021).

5.4. Paleogeographic and hydrographic environment

The paleogeographic and hydrographic backgrounds control the topography of sea-floor, terrestrial input, and water circulation in marine systems, which would further act on the primary productivity, marine stratification and (bio)geochemical cycles. In a restricted or semi-restricted basin, the stagnant water may obstruct the replenishment of major and trace elements from the open sea and contribute to redox stratification (Algeo and Rowe, 2012). Therefore, reconstruction of the Lopingian paleogeographic and hydrographic conditions could help constrain oceanic variations on both physical and chemical aspects.

From the late Middle Permian (or Guadalupian), a couple of NW-SE trending intraplatform (or intrashelf) rift subbasins, notably the Kaijiang-Liangping-Wangcang (KLW) subbasins, were initiated and generated in the northwestern margin of the Upper Yangtze Platform (Fig. 1B). Due to the temporal synchronism with the Emeishan LIP or mantle plume activity (Shellnutt et al., 2012), they were considered as having been induced by the lateral extensional process of the upper crust surrounding the Emeishan LIP in the course of mantle plume upwelling (He et al., 2003). This half-opened appendix-shaped basin configuration could have restricted the water circulation with the open ocean (Qinling or Paleo-Tethys ocean) to some extent, notably the inner part that was distal away from the outlet (Fig. 1B). The studied Xibeixiang section was located to the mouth of the KLW subbasin, where the depositional environment may be less restricted relative to the inner part.

Mo/TOC ratio is commonly used as a proxy to assess the deep-water paleo-hydrographic conditions of specific basins/shelves (Algeo and Lyons, 2006). Previous data from one upwelling zone (i.e., the Namibian Shelf) and four anoxic silled basins (i.e., the Black Sea, Framvaren Fjord, Cariaco Basin, and Saanich Inlet) revealed that Mo/TOC ratios are higher than 35×10^{-4} ppm/wt% in weakly restricted basins, and vary between 15×10^{-4} to 35×10^{-4} ppm/wt% in moderately restricted basins, and lower than 15×10^{-4} ppm/wt% in strongly restricted basins (Algeo and Lyons, 2006). Mo/TOC values from Xibeixiang Upper Permian section range from 1.37 to 101.37 ppm/wt% (mean 20.46 ppm/wt%) (Fig. 4), showing a moderately restricted environment, generally agreeing with the paleogeographic setting (Fig. 1B). Liao et al. (2019) also reported a similar Mo/TOC variation pattern in the Upper Permian in the Lower Yangtze region, pointing to a similar hydrographic setting.

Moreover, Co (ppm) × Mn (wt%) have also been used recently as the proxy for upwelling currents in modern and ancient coastal systems (Sweere et al., 2016; Zhang et al., 2018b), where the sediments deposited generally yield a low Co × Mn value (<0.4 ppm·wt%) (e.g., Peruvian Margin; Böning et al., 2004) probably in response to increasing Mn–Co removing of the upwelling Mn–Co conveyor belt (Sweere et al., 2016). Co × Mn values from Xibeixiang section are relatively high in the intervals I and IV (mean 0.27 and 0.58 ppm·wt%, respectively) (Fig. 5), indicating weak upwelling (or restricted) environments. In contrast, they turn to drop in most of intervals II and III (mean 0.20 and 0.19 ppm·wt%, respectively), likely showing enhanced upwelling currents during the two intervals. This inference are consistent with the transgression (Fig. 2) and the deposition of radiolarian-bearing siliceous rocks (Fig. 3C) in this interval.

5.5. Controls on the redox variations during the Late Permian

As documented above (Section 5.1), four intervals (or phases) are discriminated in terms of redox changes through the Late Permian to the earliest Triassic (Fig. 4). Interval I was characterized by a suboxic condition during deposition. The relative lowstand of sea level, as indicated by thick-bedded shallow water limestones bearing abundant benthic faunas (e.g., coral, brachiopod and crinoids) (Figs. 2 and 3), enabled the carbonate platform (ramp) to stand within the euphotic zone of sea surface water in which the excessive O_2 concentration and carbonate production of carbonate factory could have inhibited the organic accumulation/preservation due to the fast rate of organic decomposition and sediment dilution (Fig. 9A). On the other hand, the oligotrophic clear surface water above the carbonate platform, as reflected by the benthic oligotrophic-dominant faunal assemblages (Figs. 2 and 3) and extremely low nutrient-limiting elements (i.e., Fe, Zn, Ni, Cu) (Figs. 4 and 5), could have substantially limited the primary productivity. All these factors together may have maintained the oxygenated state of the shallow surface water (Fig. 9A).

Interval II was characterized by a euxinic state of bottom water at Xibeixiang, as indicated by the Fe speciation and RSE abundances (Fig. 4). During this interval, the relative sea level rose rapidly as evidenced by the occurrence of organic-rich marly (or argillaceous) limestones bearing pelagic fauna (Figs. 2 and 3), so that the carbonate factory was pushed down below the optimal production depth and subsequently drown in which the carbonate production was plummeted and suffocated, leading to few deposition of carbonate sediments. Meanwhile, rapid increases in the nutrient-limiting elements (i.e., Fe, Zn, Ni, Cu) into the basin (Figs. 4 and 5), probably induced by enhanced oceanic upwelling of nutrient-rich deep watermasses in the context of transgression as evidenced by the simultaneous negative shift of $\delta^{13}C_{carb}$

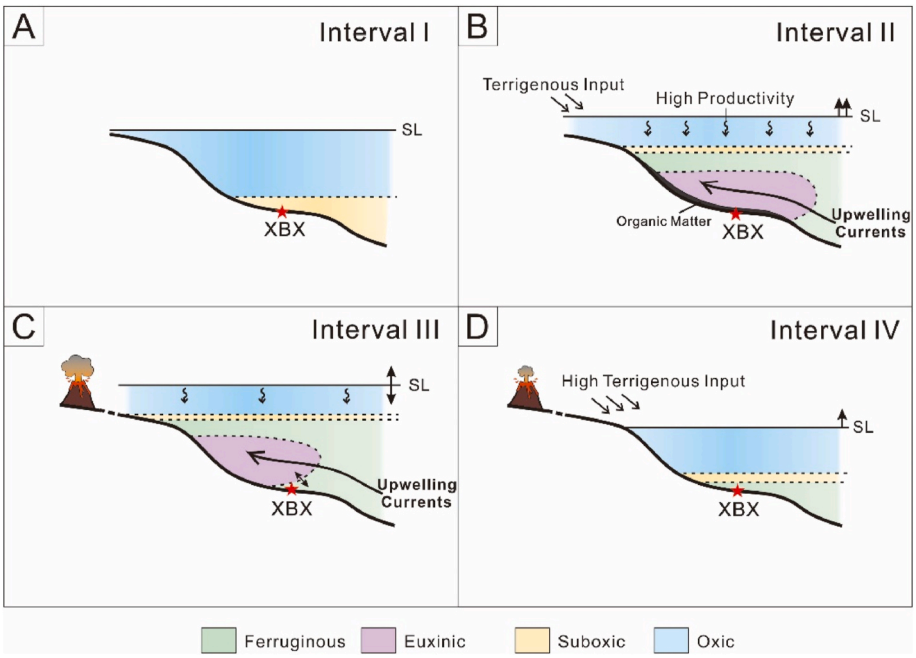

Fig. 9. Schematic diagrams showing the redox variations and controlling factors on the redox conditions in Kaijiang-Liangping-Wangcang basin during deposition of Intervals I (A), Interval II (B), Interval III (C) and Interval IV (D). This schematic illustration is not scaled. See text for detailed explanation. Abbreviations: XBX-Xibeixiang section.

(Fig. 4) and low Co × Mn values (Fig. 5), and moderate terrigenous input indicated by high Al contents (Fig. 5), could have induced the phytonplankton bloom, increasing the primary productivity and organic fluxes (Piper and Perkins, 2004). This scenario, in turn, would have increased the oxygen consumption through organic decaying, and aggravated the oxygen depletion (anoxicity) in the water column, reconciling the coeval RSE enrichment in stratigraphic column (Fig. 4). Under this circumstance, the increasing organic output/accumulation and sufficient sulfate concentration of the sea further enhanced bacterial sulfate reduction (BSR) and excessive H_2S releasing into the overlying watermass (Habicht et al., 2002; Rimmer et al., 2004). As a result, sulfidic (euxinic) watermass was created coincident with the high production zone (Fig. 9B) as seen in the stratigraphic records. This condition, on the other hand, would further favour organic preservation in sediments, at least partly contributing to the high TOC contents recorded in the stratigraphic column (Fig. 4). Similar patterns of coupled high production and anoxic (even euxinic) zones were widely reported on modern upwelling shelves and deep-time stratigraphic records (Rullkötter, 2006; Huang et al., 2019; Zhang et al., 2020b).

Interval III was dominated by ferruginous anoxic condition with intermittent incursions of euxinic water. During this interval, the relative sea level remained still high with fluctuations during the early stage and tended to drop later on as indicated by the transition from bedded cherts to thin-to medium-bedded limestones bearing ammonites (Figs. 2, 3 and 9C). On the other hand, apparent decreases in nutrient-limiting element fluxes (Fe, Zn, Ni, and Cu) to the waters (Figs. 4 and 5) could have reduced the primary productivity significantly likely driven by the slowdown of terrigenous input. Meanwhile, the decreasing organic fallouts onto the seafloor would in turn slow down the oxygen consumption and subsequent BSR, lessening the anoxicity of the water column, thus accounting for the dominance of ferruginous anoxia with intermittent euxinic spells, notably in the early stage (with a highstand sea level). In contrast, the recurrence of euxinic water column at the end of this interval might result from the downdip retreat of euxinic zone (or wedge) driven by the relative sea level drop, or volcanic-induced increases in both nutrient and sulfur fluxes, as indicated by increased occurrence of bentolite layers (Fig. 2) and sharp increases in Hg/TOC ratio (Fig. 5).

Interval IV was dominated by ferruginous anoxic state with an oxic spell just across the P-T transition, as indicated by the Fe speciation and RSE abundances (Fig. 4). During this interval, the relative sea level rose apparently after the end-interval III drop as evidenced by the occurrence of thin-bedded to platy lime mudstones intercalated with shale layers (Figs. 2 and 9D). On the other hand, the low primary productivity, as indicated by extremely low nutrient-limiting (i.e., Fe, Zn, Ni, Cu) (Figs. 4 and 5) fluxes, was likely driven by the waning of upwelling currents, agreeing with relatively high Co × Mn values (Fig. 5). These factors together could have induced the decreasing organic matter output, which ultimately reduce the oxygen consumption, and the anoxicity of watermass. Meanwhile, the abrupt high terrigenous fluxes, notably across the P-T boundary, as evidenced by high Al contents in sediments (Fig. 5), could result in the sporadic sediment dilution, thus a short oxic episode during this interval.

5.6. Comparison of redox changes during the Late Permian

In previous studies, the severest oceanic anoxia (i.e., “superanoxia”), as indicated by shallowing of the chemocline and the expansion of sulfidic (euxinic) watermasses to the surface euphotic zone, was hypothesized to be the leading cause driving the destruction of the main habitable niches and the subsequent mass extinction at the end-Permian (Riccardi et al., 2006; Shen et al., 2011). Nevertheless, numerous works demonstrated that anoxic or euxinic conditions had even occurred, dominantly during the Late Permian long before the LPME (Dolenec et al., 2001; Fio et al., 2010; Clarkson et al., 2016; Elrick et al., 2017; Lei et al., 2017; Xiang et al., 2021), only making up the prelude chapter of this severest crisis. To test the spatiotemporal extents/changes of the marine anoxia during the Late Permian, and the links to the LPME, we collect the redox data of Late Permian from different paleogeographic and paleobathymetrical settings around the world. These datasets, however, showed a high spatial heterogeneity and temporal diachroneity of the marine anoxic processes during the Late Permian, and a loose temporal link to the LPME (Fig. 10).

In Neo-Tethys regime, Ce/Ce* data from the Upper Permian

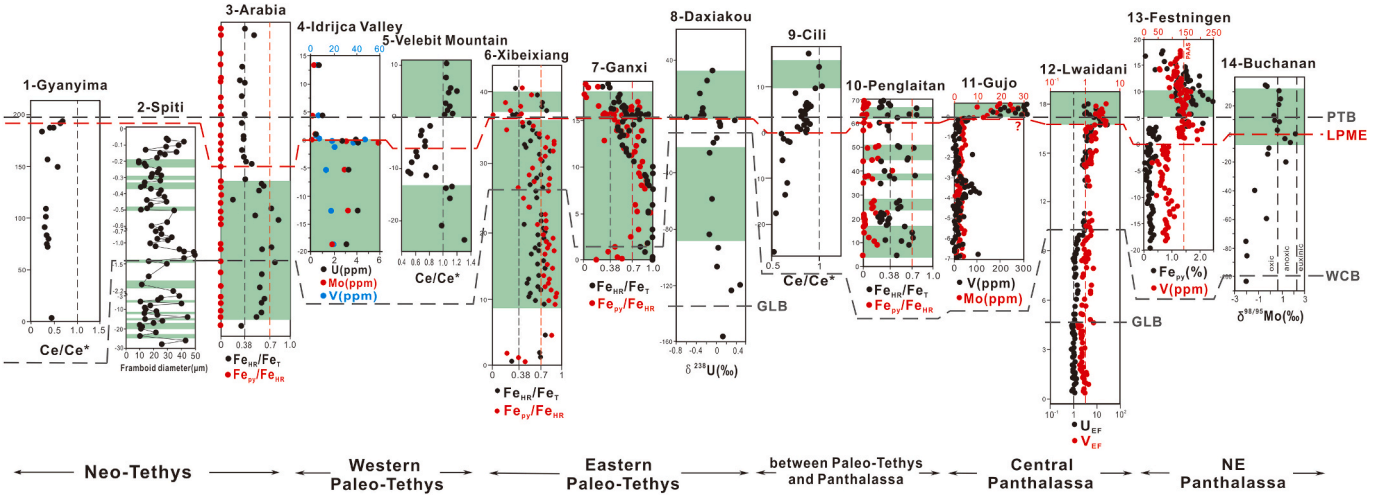

Fig. 10. Stratigraphic and paleo-redox conditions of different sections in variable backgrounds of paleogeography and paleobathemtry. Note that the green area represents anoxic conditions, and the locations of section are marked in Fig. 1A. Data sources: Gyanyima, Garbelli et al. (2016); Spiti, Stebbins et al. (2019); Arabia, Clarkson et al. (2016); Idrijca Valley, Dolenec et al. (2001); Velebit Mountain, Fio et al. (2010); Ganxi, Lei et al. (2017); Daxiakou, Elrick et al. (2017); Cili, Loope et al. (2013); Penglaitan, Xiang et al. (2021); Gujo, Algeo et al. (2011); Lwaidani, Onoue et al. (2021); Festningen, Grasby et al. (2015); Buchanan, Proemse et al. (2013). Abbreviations: PTB–Permian-Triassic boundary, LPME–Latest Permian Mass Extinction, WCB–Wuchiapingian–Changhsingian boundary, GLB-Guadalupian-Lopingian boundary. (For interpretation of the references to colour in this figure legend, the reader is referred to the Web version of this article.)

succession deposited in a carbonate platform setting on the seamount at Gyanyima, Tibet (Fig. 1 for location), indicate an oxic prevailing marine environment without signal of anoxia during the Late Permian (Garbelli et al., 2016). The Spiti section from India, located in southern Neo-Tethys (Fig. 1), comprises carbonates with black shale intercalations, representing a deeper water sedimentary environment relative to Gyanyima section. Size statistics of framboid pyrite diameter in sediments suggested only sporadic anoxia rather than a persistent anoxic condition from the late Wuchiapingian to the early-middle Changhsingian (Stebbins et al., 2019). Furthermore, iron speciation data from an Arabian section deposited from continental margin to pelagic basin in the western part of Neo-Tethys revealed that anoxia only occurred from the late Wuchiapingian to the early-middle Changhsingian, but did not occur during the LPME (Clarkson et al., 2016); whereas, data from a mid-slope section showed that the anoxic environment did not appear until the extinction interval. In contrast, data from a platform section illustrated an oxic condition during almost the entire Late Permian (Clarkson et al., 2016). Collectively, the oxic environment prevailed in the shallow seas of Neo-Tethys regime and intermittent anoxia only appeared in the mid-depth water column below the mid-slope, whilst euxinic condition did not take place completely.

However, in the western Paleo-Tethys, redox-sensitive element proxies from black carbonates at Idrijca Valley in Slovenia suggested that oceanic anoxia dominated the Late Permian, but was shifted to an oxygenated condition during the P-T interval (Dolenec et al., 2001). In contrast, Ce anomalies in dolomites of the Velebit Mountains in Croatia demonstrated an oxic condition during the Late Permian prior to the P-T transition, and the anoxia only occurred after the extinction event (Fio et al., 2010). In the eastern Paleo-Tethys, iron speciation data from both the Xibeixiang and Ganxi sections of deep-water-dominated facies show an overall anoxic condition from the late Wuchiapingian to the Early Triassic (this study; Lei et al., 2017). While U isotope data from the Daxiakou section (deposited on a carbonate ramp) proposed that the anoxic condition emerged during the mid-late Wuchiapingian and the LPME (Elrick et al., 2017). It is worth noting that a short-term oxic spell occurred across the PTB in Xibeixiang, Shangsi and Daxiakou sections (this study; Xiang et al., 2016; Elrick et al., 2017), which possibly resulted from accelerating increases in terrestrial flux and dilution due to the loss of terrestrial vegetation during the LPME (Zhang et al., 2020a). Collectively, it seems that the oceanic anoxia was more prevalent in Paleo-Tethys regime than that in the Neo-Tethys during the Late Permian and the degree of anoxia in deep-water settings was more serious than that in shallow marines (Fig. 11). Nonetheless, redox variations in pelagic basins in the middle of Paleo-Tethys remain uncertain in the absence of data.

In the Panthalassa regime (Fig. 10), in the shallow saddle portion between Paleo-Tethys and Panthalassa, Ce anomalies data from the Cili section in South China show that the watermass was oxic until the Early Triassic (Loope et al., 2013). Similarly, iron speciation data from Penglaitan, South China demonstrate sporadic oxygen deficiency during the Late Permian and predominance of oxic-suboxic in absence of euxinic watermass during the LPME (Xiang et al., 2021). Nevertheless, data from sections in Japan in central Panthalassa show different results. No anoxic watermass was generated in the Late Permian until the Early Triassic at Gujo section (Algeo et al., 2011; Fujisaki et al., 2019). In addition, redox-sensitive element (RSE) proxies from the Lwaidani section in Japan show predominance of a suboxic condition on the pelagic seafloor over the most of the Changhsingian, although aggravating near the LPME (Onoue et al., 2021). Moving to the northeastern Panthalassa (Fig. 10), Fe speciation and RSE data from Festningen section in Norway, however, show that marine anoxia only appeared during the Early Triassic (Grasby et al., 2015). With the facies deepening to the distal deep-water slope setting (Buchanan Lake, Canada), a large positive shift in $\delta^{98/95}$Mo values was discovered at the extinction horizon, consistent with the onset of anoxic conditions (Proemse et al., 2013). In contrast, Mo isotopic data from a storm-influenced shelf (West Blind Fjord,

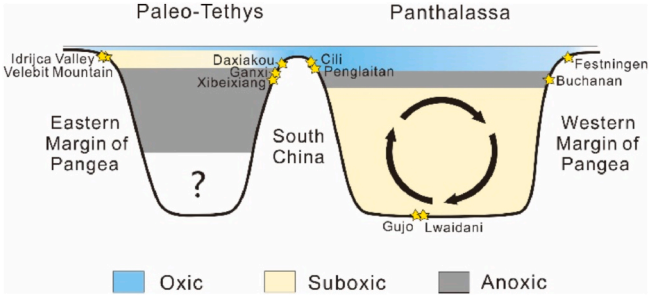

Fig. 11. Schematic W-E cross section showing the redox conditions across the Paleo-Tethys and Panthalassa during the Late Permian.

Canada) show little changes in composition, indicating a persistent oxic condition across the LPME interval (Proemse et al., 2013). In summary, as documented above, suboxic conditions predominated over pelagic basin floor in the Panthalassa regime through the Late Permian and the onsets of anoxia were diachronous depending on latitudes (Takahashi et al., 2021), while anoxic or even euxinic conditions could have impinged onto the mid-depth continental slopes, evolving updip to a complete oxic condition on the continental shelf even throughout the LPME interval.

Multiple lines of evidence have revealed apparent redox heterogeneities among the Neo-Tethys, Paleo-Tethys and Panthalassa regimes during the Late Permian (Fig. 11). Compared with the Neo-Tethys and the Panthalassa, the degree of anoxicity in the Paleo-Tethys regime was more serious, which may result from the paleogeographic contexts of the three co-existing ocean regimes during the Late Permian which could have resulted in the differences in oceanic circulation among these oceans (Fig. 1A).

The Paleo-Tethys regime was bounded by Pangea on the west, the Gondwanaland on the south, the Siberian Plate on the north and Asiatic Hunic terranes along the eastern and southern flanks of the ocean, which included the Cimmerian, South China, and North China blocks (Fig. 1A). This loop-like continent/terrane chains around the Paleo-Tethys Ocean thus could have prevented its seawater circulation with oceans outboard through which the water exchange with Panthalassa and Neo-Tethys could only take place through the narrow channels/saddles between blocks/terranes near the equator. Thus, the ocean was relatively restricted in the mid-latitudes. The magnesium isotope data of dolomite also confirm a restricted oceanic environment in the Paleo-Tethys (Hu et al., 2021). Meanwhile, without contact with the polar ice caps on both sides, the decreasing temperature difference between surface water and bottom water in the Paleo-Tethys as a result of the P-T thermal maximum (Huey and Ward, 2005; Joachimski et al., 2012; Benton and Newell, 2014; Chen et al., 2020) could have also played an important role in driving the oceanic stagnation and stratification.

From the perspective of paleogeographic contexts, the Panthalassa extended from the equator to polar regions within which the sea surface seawater could approach the ice rafts in high latitudes, causing inversions in temperature and density gradient of water column (Fig. 11), thereby enhancing the ocean circulation in the Panthalassa regime. The water exchange between the Neo-Tethys and Panthalassa could freely occur without blocking (Fig. 1A), which facilitated increasing oxygen contents in the Neo-Tethys, so that oxic conditions overwhelmingly dominated the shallow carbonate platforms/shelves from the Late Permian to the Early Triassic.

It is obvious that the onset of anoxia was diachronous in some sections. However, the timing of the mass extinction in non-hypoxic areas such as at Gyanyima in Tibet was approximately synchronous with that in other anoxic environments (Shen et al., 2010; Garbelli et al., 2016). These facts indicate that the ocean anoxia may have not acted as the exclusive killing mechanism for the organism, while the aerobic areas also did not become a refuge for organisms. Therefore, the anoxia possibly was an interactive outcome of other “precursive causes” of environmental perturbations, such as volcanic eruptions and warming (Penn et al., 2018), and then in turn exacerbated the ecosystem through interactions of other environmental forces. On the other hand, the prolonged anoxia in the Early Triassic may have delayed the restoration of the ecosystem and biotic recovery (Lau et al., 2016; Penn et al., 2018).

6. Conclusions

Detailed analyses of Fe speciation, major and trace element concentrations and mercury contents during the Late Permian are reported from Xibeixiang section, which was deposited in an intrashelf basin at the northern margin of Yangtze Block, SW China. Our data distinguish four distinct paleo-redox intervals (I-IV) based on Fe–Mo–U–V geochmiacal datasets. Of these, interval I, spanning from the upper Wuchiaping Formation to the basal Dalong Formation, was characterized by mainly an oxic-suboxic condition during deposition. Interval II (middle Dalong Formation) was dominated by euxinic conditions. Interval III, accommodating in the upper Dalong Formation, recorded a ferruginous-dominant anoxic condition interrupted by euxinic spells. Ultimately, the interval IV, spanning from the uppermost Permian to the lowermost Triassic, was dominated by a ferruginous condition with occasional incursion of oxic episode just across the P-T boundary. Moreover, the primary productivity stayed fairly low in interval I, and culminated in interval II, followed by an apparent decline in interval III, and remained lowstand in interval IV. Coincidently, the high primary productivity was temporally synchronous with the euxinic interval, so that the productivity likely played an important role in formation of the water redox states. It is noted that intensive volcanic activities as shown by concentrated tuffaceous layers and Hg/TOC anomalies occurred slightly earlier than P-T boundary, which can be well correlated with those reported at more than 20 localities over the world. Furthermore, by comparison the redox data of the Late Permian from different paleogeographic and paleobathymetrical settings around the world, we found that the paleogeographic contexts likely played a critical role in controlling the spatial heterogeneity and temporal diachroneity of the marine redox states during the Late Permian. The Paleo-Tethys was relatively restricted in oceanic circulation, thus subject to more severely anoxic condition than Neo-Tethys and Panthalassa.

Declaration of competing interest

The authors declare that they have no known competing financial interests or personal relationships that could have appeared to influence the work reported in this paper.

Acknowledgements

The authors thank Hengye Wei and Liyu Zhang for their suggestions, Hongyu Zhang, Wei Yuan and Zihu Zhang for their laboratory assistance. Constructive comments and suggestions from editor and two anonymous referees are highly acknowledged. This study was supported by the National Natural Science Foundation of China (91755210) and National Key Research and Development (R & D) Program of China (2017YFC0603103).

Appendix A. Supplementary data

Supplementary data to this article can be found online at https://doi.org/10.1016/j.marpetgeo.2022.105633.

References

Algeo, T.J., Ingall, E., 2007. Sedimentary Corg:P ratios, paleocean ventilation, and Phanerozoic atmospheric pO2. Palaeogeogr. Palaeoclimatol. Palaeoecol. 256 (3–4), 130–155.
Algeo, T.J., Kuwahara, K., Sano, H., Bates, S., Lyons, T., Elswick, E., Hinnov, L., Ellwood, B., Moser, J., Maynard, J.B., 2011. Spatial variation in sediment fluxes, redox conditions, and productivity in the Permian–Triassic Panthalassic Ocean. Palaeogeogr. Palaeoclimatol. Palaeoecol. 308 (1–2), 65–83.
Algeo, T.J., Lyons, T.W., 2006. Mo-total organic carbon covariation in modern anoxic marine environments: implications for analysis of paleoredox and paleohydrographic conditions. Paleoceanography 21 (1), 1–23.
Algeo, T.J., Maynard, J.B., 2004. Trace-element behavior and redox facies in core shales of Upper Pennsylvanian Kansas-type cyclothems. Chem. Geol. 206 (3–4), 289–318.
Algeo, T.J., Rowe, H., 2012. Paleoceanographic applications of trace-metal concentration data. Chem. Geol. 324–325, 6–18.
Amos, H.M., et al., 2014. Global biogeochemical implications of mercury discharges from rivers and sediment burial. Environ. Sci. Technol. 48 (16), 9514–9522.
Benoit, J., Gilmour, C., Mason, R., Heyes, A., 1999. Sulfide controls on mercury speciation and bioavailability to methylating bacteria in sediment pore waters. Environ. Sci. Technol. 33 (6), 951–957.
Benton, M.J., Newell, A.J., 2014. Impacts of global warming on Permo-Triassic terrestrial ecosystems. Gondwana Res. 25 (4), 1308–1337.

Berner, R.A., 2002. Examination of hypotheses for the Permo-Triassic boundary extinction by carbon cycle modeling. Proc. Natl. Acad. Sci. Unit. States Am. 99 (7), 4172–4177.
Bishop, J.K.B., 1988. The barite-opal-organic carbon association in oceanic particulate matter. Nature 332 (6162), 341–343.
Black, B.A., Lamarque, J.-F., Shields, C.A., Elkins-Tanton, L.T., Kiehl, J.T., 2014. Acid rain and ozone depletion from pulsed Siberian Traps magmatism. Geology 42 (1), 67–70.
Bond, D.P.G., Grasby, S.E., 2017. On the causes of mass extinctions. Palaeogeogr. Palaeoclimatol. Palaeoecol. 478, 3–29.
Böning, P., Brumsack, H.-J., Böttcher, M.E., Schnetger, B., Kriete, C., Kallmeyer, J., Borchers, S.L., 2004. Geochemistry of Peruvian near-surface sediments. Geochem. Cosmochim. Acta 68 (21), 4429–4451.
Bouffard, A., Amyot, M., 2009. Importance of elemental mercury in lake sediments. Chemosphere 74 (8), 1098–1103.
Bower, J., Savage, K.S., Weinman, B., Barnett, M.O., Hamilton, W.P., Harper, W.F., 2008. Immobilization of mercury by pyrite (FeS2). Environ. Pollut. 156 (2), 504–514.
Breit, G.N., Wanty, R.B., 1991. Vanadium accumulation in carbonaceous rocks: a review of geochemical controls during deposition and diagenesis. Chem. Geol. 91 (2), 83–97.
Burgess, S.D., Muirhead, J.D., Bowring, S.A., 2017. Initial pulse of Siberian Traps sills as the trigger of the end-Permian mass extinction. Nat. Commun. 8 (1), 164.
Calvert, S.E., Pedersen, T.F., 1993. Geochemistry of Recent oxic and anoxic marine sediments_ Implications for the geological record. Mar. Geol. 113 (1–2), 67–68.
Cai, X.F., Zhang, Z.F., Peng, X.F., Feng, Q.L., 2007. Depositional characteristics of hydrocarbon source rocks of the Dalong Formation and the related potential of Hubei, Hunan, Guizhou and Guangxi regions. Earth Sci. J. China Univ. Geosci. 32, 774–780 (in Chinese with English Abstract).
Canfield, D.E., 1994. Factors influencing organic carbon preservation in marine sediments. Chem. Geol. 114 (3–4), 315–329.
Canfield, D.E., Raiswell, R., Westrich, J.T., Reaves, C.M., Berner, R.A., 1986. The use of chromium reduction in the analysis of reduced inorganic sulfur in sediments and shales. Chem. Geol. 54 (1–2), 149–155.
Cao, T.T., Song, Z.G., Wang, S.B., Cao, X.X., Li, Y., Xia, J., 2015. Characterizing the pore structure in the Silurian and permian shales of the Sichuan Basin, China. Mar. Petrol. Geol. 61, 140–150.
Cappellen, P.V., Ingall, E.D., 1994. Benthic phosphorus regeneration, net primary production, and ocean anoxia: a model of the coupled marine biogeochemical cycles of carbon and phosphorus. Paleoceanography 9 (5), 677–692.
Charbonnier, G., Godet, A., Bodin, S., Adatte, T., Föllmi, K.B., 2018. Mercury anomalies, volcanic pulses, and drowning episodes along the northern Tethyan margin during the latest Hauterivian-earliest Aptian. Palaeogeogr. Palaeoclimatol. Palaeoecol. 505, 337–350.
Chen, J., Shen, S.Z., Zhang, Y.C., Angiolini, L., Gorgij, M.N., Crippa, G., Wang, W., Zhang, H., Yuan, D.X., Li, X.H., Xu, Y.G., 2020. Abrupt warming in the latest Permian detected using high-resolution in situ oxygen isotopes of conodont apatite from Abadeh, central Iran. Palaeogeogr. Palaeoclimatol. Palaeoecol. 560, 109973.
Clarkson, M.O., Kasemann, S.A., Wood, R.A., Lenton, T.M., Daines, S.J., Richoz, S., Ohnemueller, F., Meixner, A., Poulton, S.W., Tipper, E.T., 2015. Ocean acidification and the Permo-Triassic mass extinction. Science 348 (6231), 229–232.
Clarkson, M.O., Poulton, S.W., Guilbaud, R., Wood, R.A., 2014. Assessing the utility of Fe/Al and Fe-speciation to record water column redox conditions in carbonate-rich sediments. Chem. Geol. 382, 111–122.
Clarkson, M.O., Wood, R.A., Poulton, S.W., Richoz, S., Newton, R.J., Kasemann, S.A., Bowyer, F., Krystyn, L., 2016. Dynamic anoxic ferruginous conditions during the end-Permian mass extinction and recovery. Nat. Commun. 7, 12236.
Dehairs, F., Baeyens, W., Goeyens, L., 1992. Accumulation of suspended barite at mesopelagic depths and export production in the Southern Ocean. Science 258 (5086), 1332–1335.
Dehairs, F., Chesselet, R., Jedwab, J., 1980. Discrete suspended particles of barite and the barium cycle in the open ocean. Earth Planet Sci. Lett. 49 (2), 528–550.
Dehairs, F., Lambert, C.E., Chesselet, R., Risler, N., 1987. The biological production of marine suspended barite and the barium cycle in the Western Mediterranean Sea. Biogeochemistry 4 (2), 119–140.
Dolenec, T., Lojen, S., Ramovš, A., 2001. The Permian–Triassic boundary in Western Slovenia (Idrijca Valley section): magnetostratigraphy, stable isotopes, and elemental variations. Chem. Geol. 175 (1–2), 175–190.
Duan, Y.H., Han, D.S., Batchelor, B., Abdel-Wahab, A., 2016. Synthesis, characterization, and application of pyrite for removal of mercury. Colloids Surf. A Physicochem. Eng. Asp. 490, 326–335.
Dymond, J., Suess, E., Lyle, M., 1992. Barium in deep-sea sediment: a geochemical proxy for paleoproductivity. Paleoceanography 7 (2), 163–181.
Elrick, M., Polyak, V., Algeo, T.J., Romaniello, S., Asmerom, Y., Herrmann, A.D., Anbar, A.D., Zhao, L., Chen, Z.-Q., 2017. Global-ocean redox variation during the middle-late Permian through Early Triassic based on uranium isotope and Th/U trends of marine carbonates. Geology 45 (2), 163–166.
Erwin, D.H., Bowring, S.A., Yugan, J., 2002. End-Permian mass extinctions: a review. Geol. Soc. Am. Bull. 356, 363–383.
Filippelli, G.M., Delaney, M.L., 1996. Phosphorus geochemistry of equatorial Pacific sediments. Geochem. Cosmochim. Acta 60 (9), 1479–1495.
Fio, K., Spangenberg, J.E., Vlahović, I., Sremac, J., Velić, I., Mrinjek, E., 2010. Stable isotope and trace element stratigraphy across the Permian–Triassic transition: a redefinition of the boundary in the Velebit Mountain, Croatia. Chem. Geol. 278 (1–2), 38–57.
Fujisaki, W., Sawaki, Y., Matsui, Y., Yamamoto, S., Isozaki, Y., Maruyama, S., 2019. Redox condition and nitrogen cycle in the Permian deep mid-ocean: a possible contrast between Panthalassa and Tethys. Global Planet. Change 172, 179–199.
Gao, Q.L., Zhang, N., Xia, W.C., Feng, Q.L., Chen, Z.Q., Zheng, J.P., Griffin, W.L., O'Reilly, S.Y., Pearson, N.J., Wang, G.Q., Wu, S., Zhong, W.L., Sun, X.F., 2013. Origin of volcanic ash beds across the Permian–Triassic boundary, Daxiakou, South China: petrology and U–Pb age, trace elements and Hf-isotope composition of zircon. Chem. Geol. 360–361, 41–53.
Garbelli, C., Angiolini, L., Brand, U., Shen, S.-z., Jadoul, F., Posenato, R., Azmy, K., Cao, C.-q., 2016. Neotethys seawater chemistry and temperature at the dawn of the end Permian mass extinction. Gondwana Res. 35, 272–285.
Gill, G.A., Fitzgerald, W.F., 1988. Vertical mercury distributions in the oceans. Geochem. Cosmochim. Acta 52 (6), 1719–1728.
Grasby, S.E., Beauchamp, B., 2009. Latest permian to early triassic basin-to-shelf anoxia in the Sverdrup basin, Arctic Canada. Chem. Geol. 264 (1–4), 232–246.
Grasby, S.E., Beauchamp, B., Bond, D.P.G., Wignall, P., Talavera, C., Galloway, J.M., Piepjohn, K., Reinhardt, L., Blomeier, D., 2015. Progressive environmental deterioration in northwestern Pangea leading to the latest Permian extinction. Geol. Soc. Am. Bull. 127 (9–10), 1331–1347.
Grasby, S.E., Sanei, H., Beauchamp, B., Chen, Z., 2013. Mercury deposition through the permo–triassic biotic crisis. Chem. Geol. 351, 209–216.
Grasby, S.E., Shen, W., Yin, R., Gleason, J.D., Blum, J.D., Lepak, R.F., Hurley, J.P., Beauchamp, B., 2017. Isotopic signatures of mercury contamination in latest Permian oceans. Geology 45 (1), 55–58.
Grasby, S.E., Them, T.R., Chen, Z., Yin, R., Ardakani, O.H., 2019. Mercury as a proxy for volcanic emissions in the geologic record. Earth Sci. Rev. 196, 1–16.
Grice, K., Cao, C., Love, G.D., Bottcher, M.E., Twitchett, R.J., Grosjean, E., Summons, R. E., Turgeon, S.C., Dunning, W., Jin, Y., 2005. Photic zone euxinia during the Permian-triassic superanoxic event. Science 307 (5710), 706–709.
Habicht, K.S., Gade, M., Thamdrup, B., Berg, P., Canfield, D.E., 2002. Calibration of sulfate levels in the Archean ocean. Science 298, 2372–2374.
Han, D.S., Orillano, M., Khodary, A., Duan, Y., Batchelor, B., Abdel-Wahab, A., 2014. Reactive iron sulfide (FeS)-supported ultrafiltration for removal of mercury (Hg(II)) from water. Water Res. 53, 310–321.
He, B., Xu, Y.G., Xiao, L., Wang, K.M., Sha, S.L., 2003. The formation mechanism and spatial distribution of the Emeishan large igneous province: new evidences from sedimentary stratigraphy. Acta Geol. Sin. 77 (2) (in Chinese with English Abstract).
Hinojosa, J.L., Brown, S.T., Chen, J., DePaolo, D.J., Paytan, A., Shen, S.-z., Payne, J.L., 2012. Evidence for end-Permian ocean acidification from calcium isotopes in biogenic apatite. Geology 40 (8), 743–746.
Ho, P., Lee, J.-M., Heller, M.I., Lam, P.J., Shiller, A.M., 2018. The distribution of dissolved and particulate Mo and V along the U.S. GEOTRACES East Pacific Zonal Transect (GP16): the roles of oxides and biogenic particles in their distributions in the oxygen deficient zone and the hydrothermal plume. Mar. Chem. 201, 242–255.
Holmes, C.D., Jacob, D.J., Corbitt, E.S., Mao, J., Yang, X., Talbot, R., Slemr, F., 2010. Global atmospheric model for mercury including oxidation by bromine atoms. Atmos. Chem. Phys. 10 (24), 12037–12057.
Hu, Z.Y., Li, W.Q., Zhang, H., Krainer, K., Zheng, Q.F., Xia, Z.G., Hu, W.X., Shen, S.Z., 2021. Mg isotope evidence for restriction events within the Paleotethys ocean around the Permian-Triassic transition. Earth Planet Sci. Lett. 556, 116704.
Huang, T.Y., Chen, D.Z., Fu, Y., Yeasmin, R., Guo, C., 2019. Development and evolution of a euxinic wedge on the ferruginous outer shelf of the early Cambrian Yangtze sea. Chem. Geol. 524, 259–271.
Huey, R.B., Ward, P.D., 2005. Hypoxia, global warming, and terrestrial late permian extinctions. Science 308 (5720), 398–401.
Isozaki, Y., 1997. Permo-Triassic boundary superanoxia and stratified superocean: records from lost deep sea. Science 276 (5310), 235–238.
Joachimski, M.M., Lai, X., Shen, S., Jiang, H., Luo, G., Chen, B., Chen, J., Sun, Y., 2012. Climate warming in the latest Permian and the Permian-Triassic mass extinction. Geology 40 (3), 195–198.
Lau, K.V., Maher, K., Altiner, D., Kelley, B.M., Kump, L.R., Lehrmann, D.J., Silva-Tamayo, J.C., Weaver, K.L., Yu, M., Payne, J.L., 2016. Marine anoxia and delayed Earth system recovery after the end-Permian extinction. Proc. Natl. Acad. Sci. U. S. A. 113 (9), 2360–2365.
Lei, L.D., Shen, J., Li, C., Algeo, T.J., Chen, Z.Q., Feng, Q.L., Cheng, M., Jin, C.S., Huang, J.H., 2017. Controls on regional marine redox evolution during Permian-Triassic transition in South China. Palaeogeogr. Palaeoclimatol. Palaeoecol. 486, 17–32.
Liao, Z.W., Hu, W.X., Cao, J., Wang, X.L., Hu, Z.Y., 2019. Petrologic and geochemical evidence for the formation of organic-rich siliceous rocks of the Late Permian Dalong Formation, Lower Yangtze region, southern China. Mar. Petrol. Geol. 103, 41–54.
Loope, G.R., Kump, L.R., Arthur, M.A., 2013. Shallow water redox conditions from the Permian–Triassic boundary microbialite: the rare earth element and iodine geochemistry of carbonates from Turkey and South China. Chem. Geol. 351, 195–208.
Luo, J.X., He, Y.B., 2011. Anoxic environments of the permian of middle and upper Yangtze area. J. Palaeogeogr. 13, 11–20 (in Chinese with English Abstract).
Mei, S., M. Henderson, C., 2001. Evolution of Permian conodont provincialism and its significance in global correlation and paleoclimate implication. Palaeogeogr. Palaeoclimatol. Palaeoecol. 170 (3–4), 237–260.
Nielsen, J.K., Shen, Y., 2004. Evidence for sulfidic deep water during the late permian in the east Greenland basin. Geology 32 (12), 1037–1040.
Onoue, T., Soda, K., Isozaki, Y., 2021. Development of deep-sea anoxia in Panthalassa during the Lopingian (late permian): insights from redox-sensitive elements and multivariate analysis. Front. Earth Sci. 8, 213126.

Payne, J.L., Turchyn, A.V., Paytan, A., Depaolo, D.J., Lehrmann, D.J., Yu, M., Wei, J., 2010. Calcium isotope constraints on the end-Permian mass extinction. Proc. Natl. Acad. Sci. U. S. A. 107 (19), 8543–8548.
Pedersen, T.F., Calvert, S.E., 1990. Anoxia vs. Productivity: What Controls the Formation of Organic-Carbon-Rich Sediments and Sedimentary Rocks? AAPG Bulletin 74 (4), 454–466.
Penn, J.L., Deutsch, C., Payne, J.L., Sperling, E.A., 2018. Temperature-dependent hypoxia explains biogeography and severity of end-Permian marine mass extinction. Science 362 (6419), 1–6.
Percival, L.M.E., Ruhl, M., Hesselbo, S.P., Jenkyns, H.C., Mather, T.A., Whiteside, J.H., 2017. Mercury evidence for pulsed volcanism during the end-Triassic mass extinction. Proc. Natl. Acad. Sci. U. S. A. 114 (30), 7929–7934.
Percival, L.M.E., Witt, M.L.I., Mather, T.A., Hermoso, M., Jenkyns, H.C., Hesselbo, S.P., Al-Suwaidi, A.H., Storm, M.S., Xu, W., Ruhl, M., 2015. Globally enhanced mercury deposition during the end-pliensbachian extinction and Toarcian OAE: a link to the Karoo–Ferrar large igneous province. Earth Planet Sci. Lett. 428, 267–280.
Piper, D.Z., Calvert, S.E., 2009. A marine biogeochemical perspective on black shale deposition. Earth Sci. Rev. 95 (1–2), 63–96.
Piper, D.Z., Perkins, R.B., 2004. A modern vs. Permian black shale—the hydrography, primary productivity, and water-column chemistry of deposition. Chem. Geol. 206 (3–4), 177–197.
Pirrone, N., Cinnirella, S., Feng, X., Finkelman, R.B., Friedli, H.R., Leaner, J., Mason, R., Mukherjee, A.B., Stracher, G.B., Streets, D.G., Telmer, K., 2010. Global mercury emissions to the atmosphere from anthropogenic and natural sources. Atmos. Chem. Phys. 10 (13), 5951–5964.
Poulton, S.W., Canfield, D.E., 2005a. Development of a sequential extraction procedure for iron: implications for iron partitioning in continentally derived particulates. Chem. Geol. 214 (3–4), 209–221.
Poulton, S.W., Canfield, D.E., 2011. Ferruginous conditions: a dominant Feature of the ocean through Earth's history. Elements 7, 107–112.
Poulton, S.W., Canfield, D.E.J.C.G., 2005b. Development of a sequential extraction procedure for iron: implications for iron partitioning in continentally derived particulates. Chem. Geol. 214 (3), 209–221.
Proemse, B.C., Grasby, S.E., Wieser, M.E., Mayer, B., Beauchamp, B., 2013. Molybdenum isotopic evidence for oxic marine conditions during the latest Permian extinction. Geology 41 (9), 967–970.
Ravichandran, M., 2004. Interactions between mercury and dissolved organic matter–a review. Chemosphere 55 (3), 319–331.
Riccardi, A.L., Arthur, M.A., Kump, L.R., 2006. Sulfur isotopic evidence for chemocline upward excursions during the end-Permian mass extinction. Geochem. Cosmochim. Acta 70 (23), 5740–5752.
Rimmer, S.M., Thompson, J.A., Goodnight, S.A., Robl, T.L., 2004. Multiple controls on the preservation of organic matter in Devonian–Mississippian marine black shales: geochemical and petrographic evidence. Palaeogeogr. Palaeoclimatol. Palaeoecol. 215 (1–2), 125–154.
Rullkötter, J., 2006. Organic matter: the driving Force for early diagenesis. In: Schulz, H. D., Zabel, M. (Eds.), Marine Geochemistry, pp. 169–206. Springer, Berlin, Heidelberg.
Sanei, H., Grasby, S.E., Beauchamp, B., 2011. Latest Permian mercury anomalies. Geology 40 (1), 63–66.
Scaife, J.D., Ruhl, M., Dickson, A.J., Mather, T.A., Jenkyns, H.C., Percival, L.M.E., Hesselbo, S.P., Cartwright, J., Eldrett, J.S., Bergman, S.C., Minisini, D., 2017. Sedimentary mercury enrichments as a marker for submarine large igneous province volcanism? Evidence from the mid-Cenomanian event and oceanic anoxic event 2 (late Cretaceous). G-cubed 18, 4253–4275.
Schenau, S.J., Lange, G.J.D., 2001. Phosphorus regeneration vs. burial in sediments of the Arabian Sea. Mar. Chem. 75 (3), 201–217.
Schenau, S.J., Reichart, G.J., De Lange, G.J., 2005. Phosphorus burial as a function of paleoproductivity and redox conditions in Arabian Sea sediments. Geochem. Cosmochim. Acta 69 (4), 919–931.
Schmitz, B., 1987. Barium, equatorial high productivity, and the northward wandering of the Indian continent. Paleoceanography 2 (1), 63–77.
Schoepfer, S.D., Shen, J., Wei, H., Tyson, R.V., Ingall, E., Algeo, T.J., 2015. Total organic carbon, organic phosphorus, and biogenic barium fluxes as proxies for paleomarine productivity. Earth Sci. Rev. 149, 23–52.
Scholz, F., 2018. Identifying oxygen minimum zone-type biogeochemical cycling in Earth history using inorganic geochemical proxies. Earth Sci. Rev. 184, 29–45.
Scholz, F., Siebert, C., Dale, A.W., Frank, M., 2017. Intense molybdenum accumulation in sediments underneath a nitrogenous water column and implications for the reconstruction of paleo-redox conditions based on molybdenum isotopes. Geochem. Cosmochim. Acta 213, 400–417.
Scott, C., Lyons, T.W., 2012. Contrasting molybdenum cycling and isotopic properties in euxinic versus non-euxinic sediments and sedimentary rocks: refining the paleoproxies. Chem. Geol. 324–325, 19–27.
Selin, N.E., 2009. Global biogeochemical cycling of mercury: a review. Annu. Rev. Environ. Resour. 34 (1), 43–63.
Sepkoski, J.J., 2016. A kinetic model of Phanerozoic taxonomic diversity. III. Post-Paleozoic families and mass extinctions. Paleobiology 10 (2), 246–267.
Shellnutt, J.G., Denyszyn, S.W., Mundil, R., 2012. Precise age determination of mafic and felsic intrusive rocks from the Permian Emeishan large igneous province (SW China). Gondwana Res. 22 (1), 118–126.
Shen, J., Algeo, T.J., Planavsky, N.J., Yu, J.X., Feng, Q.L., Song, H.J., Song, H.Y., Rowe, H., Zhou, L., Chen, J.B., 2019a. Mercury enrichments provide evidence of Early Triassic volcanism following the end-Permian mass extinction. Earth Sci. Rev. 195, 191–212.
Shen, J., Chen, J., Algeo, T.J., Yuan, S., Feng, Q., Yu, J., Zhou, L., O'Connell, B., Planavsky, N.J., 2019b. Evidence for a prolonged Permian-Triassic extinction interval from global marine mercury records. Nat. Commun. 10 (1), 1–9.
Shen, S.Z., Cao, C.Q., Zhang, Y.C., Li, W.Z., Shi, G.R., Wang, Y., Wu, Y.S., Ueno, K., Henderson, C.M., Wang, X.D., Zhang, H., Wang, X.J., Chen, J., 2010. End-Permian mass extinction and palaeoenvironmental changes in Neotethys: evidence from an oceanic carbonate section in southwestern Tibet. Global Planet. Change 73 (1–2), 3–14.
Shen, Y., Farquhar, J., Zhang, H., Masterson, A., Zhang, T., Wing, B.A., 2011. Multiple S-isotopic evidence for episodic shoaling of anoxic water during Late Permian mass extinction. Nat. Commun. 2, 1–5.
Sial, A.N., Chen, J., Lacerda, L.D., Frei, R., Tewari, V.C., Pandit, M.K., Gaucher, C., Ferreira, V.P., Cirilli, S., Peralta, S., Korte, C., Barbosa, J.A., Pereira, N.S., 2016. Mercury enrichment and Hg isotopes in Cretaceous–Paleogene boundary successions: links to volcanism and palaeoenvironmental impacts. Cretac. Res. 66, 60–81.
Scotese, C.R., Langford, R.P., 1995. Pangea and the paleogeography of the permian. In: Scholle, A., Peryt, T.M., Ulmer-Scholle, D.A. (Eds.), The Permian of Northern Pangea, vol. 1. Springer, Berlin, pp. 3–19.
Scotese, C.R., 2016. PALEOMAP PaleoAtlas for GPlates and the PaleoData Plotter Program. PALEOMAP Project. http://www.earthbyte.org/paleomap-paleoatlas-for gplates/.
Stebbins, A., Williams, J., Brookfield, M., Nye, S.W., Hannigan, R., 2019. Frequent euxinia in southern Neo-Tethys Ocean prior to the end-Permian biocrisis: evidence from the Spiti region, India. Palaeogeogr. Palaeoclimatol. Palaeoecol. 516, 1–10.
Svensen, H., Planke, S., Polozov, A.G., Schmidbauer, N., Corfu, F., Podladchikov, Y.Y., Jamtveit, B., 2009. Siberian gas venting and the end-Permian environmental crisis. Earth Planet Sci. Lett. 277 (3–4), 490–500.
Sweere, T., van den Boorn, S., Dickson, A.J., Reichart, G.-J., 2016. Definition of new trace-metal proxies for the controls on organic matter enrichment in marine sediments based on Mn, Co, Mo and Cd concentrations. Chem. Geol. 441, 235–245.
Takahashi, S., Hori, R.S., Yamakita, S., Aita, Y., Takemura, A., Ikehara, M., Xiong, Y., Poulton, S.W., Wignall, P.B., Itai, T., Campbell, H.J., Spörli, B.K., 2021. Progressive Development of Ocean Anoxia in the End-Permian Pelagic Panthalassa: Global and Planetary Change, vol. 207.
Takahashi, S., Yamasaki, S.-i., Ogawa, Y., Kimura, K., Kaiho, K., Yoshida, T., Tsuchiya, N., 2014. Bioessential element-depleted ocean following the euxinic maximum of the end-Permian mass extinction. Earth Planet Sci. Lett. 393, 94–104.
Taylor, S., Mclennan, S.M., 1985. The Continental Crust: its Composition and Evolution. Blackwell, Malden, Mass.
Thibodeau, A.M., Ritterbush, K., Yager, J.A., West, A.J., Ibarra, Y., Bottjer, D.J., Berelson, W.M., Bergquist, B.A., Corsetti, F.A., 2016. Mercury anomalies and the timing of biotic recovery following the end-Triassic mass extinction. Nat. Commun. 7, 1–8.
Tribovillard, N., Algeo, T.J., Lyons, T., Riboulleau, A., 2006. Trace metals as paleoredox and paleoproductivity proxies: an update. Chem. Geol. 232 (1–2), 12–32.
Tyson, R.V., 2005. The "productivity versus preservation" controversy: cause, flaws, and resolution. Soc. Sediment. Geol. 82, 17–33.
Tyson, R.V., Pearson, T.H., 1991. Modern and ancient continental shelf anoxia: an overview. Geol. Soc. Lond., Spec. Publ. 58 (1), 1–24.
Wang, J.G., Chen, D.Z., Yan, D.T., Wei, H.Y., Xiang, L., 2012. Evolution from an anoxic to oxic deep ocean during the Ediacaran–Cambrian transition and implications for bioradiation. Chem. Geol. 306–307, 129–138.
Wang, X.D., Cawood, P.A., Zhao, H., Zhao, L.S., Grasby, S.E., Chen, Z.Q., Wignall, P.B., Lv, Z.Y., Han, C., 2018b. Mercury anomalies across the end Permian mass extinction in South China from shallow and deep water depositional environments. Earth Planet Sci. Lett. 496, 159–167.
Wang, X.D., Cawood, P.A., Zhao, H., Zhao, L.S., Grasby, S.E., Chen, Z.Q., Zhang, L., 2019. Global mercury cycle during the end-Permian mass extinction and subsequent Early Triassic recovery. Earth Planet Sci. Lett. 513, 144–155.
Wang, M., Zhong, Y.T., Hou, Y.L., Shen, S.Z., Xu, Y.G., He, B., 2018a. Source and extent of the felsic volcanic ashes at the Permian-Triassic boundary in South China. Acta Petrol. Sin. 34 (1), 36–48 (in Chinese with English Abstract).
Wanty, R.B., Goldhaber, M.B., 1992. Thermodynamics and kinetics of reactions involving vanadium in natural systems_ Accumulation of vanadium in sedimentary rocks. Geochem. Cosmochim. Acta 56 (4), 1471–1483.
Wei, Z.F., Wang, Y.L., Wang, G., Sun, Z.P., Xu, L., 2018. Pore characterization of organic-rich late permian Da-long Formation shale in the Sichuan Basin, southwestern China. Fuel 211, 507–516.
Wignall, P.B., Hallam, A., Xulong, L., Fengqing, Y., 1995. Palaeoenvironmental changes across the permian/triassic boundary at Shangsi (N. Sichuan, China). Hist. Biol. 10 (2), 175–189.
Xiang, L., Schoepfer, S.D., Yuan, D.-X., Zheng, Q.-F., Zhang, H., 2021. Oceanic redox evolution across the end-Permian mass extinction at Penglaitan section, South China. Palaeoworld 31 (1), 93–102.
Xiang, L., Schoepfer, S.D., Zhang, H., Yuan, D.X., Cao, C.Q., Zheng, Q.F., Henderson, C. M., Shen, S.Z., 2016. Oceanic redox evolution across the end-Permian mass extinction at Shangsi, South China. Palaeogeogr. Palaeoclimatol. Palaeoecol. 448, 59–71.
Yan, J.X., Ma, Z.X., Xie, X.N., Xue, W.Q., Li, B., Liu, D.Q., 2008. Subdivision of Permian Fossil Communities and Habitat Types in Northeast Sichuan, South China. Journal of China University of Geosciences 19 (5), 441–450.
Yuan, Y.Y., Cai, C.F., Wang, T.K., Xiang, L., Jia, L.Q., Chen, Y., 2014. Redox condition during Ediacaran–Cambrian transition in the Lower Yangtze deep water basin, South China: constraints from iron speciation and δ 13Corg in the Diben section, Zhejiang. Chin. Sci. Bull. 59 (28), 3638–3649.

Zhang, B.L., Yao, S.P., Wignall, P.B., Hu, W.X., Ding, H., Liu, B., Ren, Y.L., 2018a. Widespread coastal upwelling along the eastern paleo-Tethys margin (south China) during the middle permian (Guadalupian): implications for organic matter accumulation. Mar. Petrol. Geol. 97, 113–126.

Zhang, F.F., Shen, S.Z., Cui, Y., Lenton, T.M., Dahl, T.W., Zhang, H., Zheng, Q.F., Wang, W.Q., Krainer, K., Anbar, A.D., 2020a. Two distinct episodes of marine anoxia during the Permian-Triassic crisis evidenced by uranium isotopes in marine dolostones. Geochem. Cosmochim. Acta 287, 165–179.

Zhang, G.J., Chen, D.Z., Ding, Y., Huang, T.Y., 2020b. Redox fluctuations and organic accumulation on the outer shelf of the Early Cambrian (Ages 2–3) Yangtze sea: Geochemical records on a seaward submarine sill. Geological Journal 56 (4), 1841–1857.

Zhang, H., Zhang, F.F., Chen, J.B., Douglas, H.E., Drew, D.S., Ni, P., Michael, R., Chi, Z., Cai, Y.F., Xiang, L., Li, W.Q., Liu, S.A., Wang, R.C., Wang, X.D., Feng, Z., Li, H.M., Zhang, T., Cai, H.M., Zheng, W., Cui, Y., Zhu, X.K., Hou, Z.Q., Wu, F.Y., Xu, Y.G., Noah, P., Shen, S.Z., 2021. Felsic volcanism as a factor driving the end-Permian mass extinction. Sci. Adv. 7 (47), 1–13.

Zhang, L.J., Buatois, L.A., Mángano, M.G., Gong, Y.M., Feng, Q.L., Qi, Y.A., Luo, M., Zhang, X., 2018b. Uppermost Permian trace fossils along a shelf to slope transect in South China and their implications for oceanic redox evolution and extinction pattern. Global Planet. Change 167, 74–86.

Zhao, T.Y., Algeo, T.J., Feng, Q.L., Zi, J.W., Xu, G.Z., 2019. Tracing the provenance of volcanic ash in Permian–Triassic boundary strata, South China: constraints from inherited and syn-depositional magmatic zircons. Palaeogeogr. Palaeoclimatol. Palaeoecol. 516, 190–202.